

Non-Passive Transport of Volatile Organic Compounds in the Unsaturated Zone

Orlando Silva and Jordi Grifoll*

Departament d'Enginyeria Química,
Escola Tècnica Superior d'Enginyeria Química (ETSEQ),
Universitat Rovira i Virgili,
Av. dels Països Catalans 26,
43007 Tarragona, Spain.

*Corresponding author. Tel.: +34 977 55 96 39; fax +34 977 55 96 21

E-mail addresses:

orlando.silva@urv.cat (O. Silva), jordi.grifoll@urv.cat (J. Grifoll)

1 **Abstract**

2

3 A detailed model was formulated to describe the non-passive transport of water-soluble
4 chemicals in the unsaturated zone and used to illustrate one-dimensional infiltration and
5 redistribution of alcohol-water mixtures. The model includes the dependence of density,
6 viscosity, surface tension, molecular diffusion coefficient in the liquid phase, and gas-liquid
7 partition coefficient on the aqueous mixture composition. It also takes into account the
8 decrease in the gas-liquid partition coefficient at high capillary pressures, in accordance with
9 Kelvin's equation for multi-component mixtures. Simulation of butanol-water mixtures
10 infiltration in sand was in agreement with the experimental data and simulations reported in
11 the literature. Simulation of methanol infiltration and redistribution in two different soils
12 showed that methanol concentration significantly affects volumetric liquid content and
13 concentration profiles, as well as the normalized volatilization and evaporation fluxes.
14 Dispersion in the liquid-phase was the predominant mechanism in the transport of methanol
15 when dispersivity at saturation was set to 7.8 cm. Liquid flow was mainly due to capillary
16 pressure gradients induced by changes in volumetric liquid content. However, for dispersivity
17 at saturation set to 0.2 cm, changes in surface tension due to variation in composition induced
18 important liquid flow and convection in the liquid-phase was the most active transport
19 mechanism. When the Kelvin effect was ignored within the soil, the gas-phase diffusion was
20 significantly lower, leading to lower evaporation flux of water and higher volumetric liquid
21 contents near the soil surface.

22

23 **1. Introduction**

24

25 Most numerical models of flow and transport through the vadose zone assume that flow is
26 independent of solute concentration. However, the presence of some chemicals in water can
27 affect the physical properties of the fluid phases, and the resulting transport processes are
28 known as non-passive. Thus, modeling of infiltration, redistribution and
29 volatilization/evaporation of these aqueous mixtures should take into account their non-
30 passive transport behavior.

31 Various authors have already considered the dependence of some properties on
32 concentration. For example, Boufadel et al. [6] developed a one-dimensional model to
33 simulate the density-dependent flow of salt water in variably saturated media. They found that
34 the concentration at the front and the flux front position and magnitude propagate faster in the
35 case of density-dependent solutions than in the case of passive transport. In a later study,
36 Boufadel et al. [7] expanded their model to take into account density-and-viscosity-dependent
37 flow in two-dimensional variably saturated porous media and used it to investigate beach
38 hydraulics at seawater concentration in the context of nutrient delivery for bioremediation of
39 oil spills on beaches. Numerical simulations applied to a rectangular section of a hypothetical
40 beach showed that buoyancy in the unsaturated zone is significant in anisotropic fine-textured
41 soils with low dispersivities. In all the cases considered, the effects of concentration-
42 dependent viscosity were negligible compared to the effects of concentration-dependent
43 density. Ouyang and Zheng [33] used the model FEMWATER to simulate the transport of
44 two chemicals, one with relatively low water solubility (aldicarb) and the other with relatively
45 high water solubility (acephate), through an unsaturated sandy soil. Comparison of
46 simulations showed that the effects of solution density on the transport of aldicarb were
47 negligible, whereas acephate, with density-driven transport, migrated 22 % deeper into the

48 soil in a period of 90 days than without considering density-driven transport. They also
49 performed a numerical experiment including a viscosity-concentration relationship, but the
50 results indicated that the effect of the viscosity was negligible compared with the effect of
51 density for the simulation conditions used in their study. The study of Ouyang and Zheng [33]
52 suggested that under certain circumstances, e.g. high chemical concentration, high water
53 solubility, and high pure chemical density, exclusion of the density-induced mechanism could
54 result in inaccurate predictions of water movement and chemical leaching through the vadose
55 zone. These usual simplifications could also lead to inadequate interaction between the
56 different mass transfer mechanisms when they are included in modeling of transport through
57 reactive soils. As Zhang et al. [48] pointed out, concentrated aqueous solutions are
58 significantly different from dilute solutions in transport and geochemical processes because of
59 their large density, viscosity, and complicated ionic interactions.

60 A number of studies of the effects induced on the flow by surfactants have emphasized their
61 non-passive transport behavior in the vadose zone. Smith and Gillham [43] developed an
62 isothermal saturated-unsaturated flow and transport model with solute concentration-
63 dependent surface tension. They applied the model to simulate the infiltration of aqueous
64 solutions of butanol and methanol into two soils with different silt contents. Their numerical
65 simulations indicated that solutes that depress surface tension cause a local increase in the
66 hydraulic head gradients, which increases the liquid fluxes and the solute transport. Smith and
67 Gillham [44] complemented their previous work with laboratory experiments conducted in
68 saturated-unsaturated column sand. In this second work, they also incorporated the effect of
69 concentration-dependent viscosity into their earlier model [43] to scale the unsaturated
70 hydraulic conductivity. From their experimental data and numerical simulations, they
71 distinguished two flow effects associated with concentration-dependent surface tension in the
72 vadose zone: (i) the transient unsaturated flow caused by changes in pressure head, and (ii) a

73 decrease in the height of the capillary fringe. Both effects were proportional to the changes in
74 the relative surface tension with solute concentration. They also observed that higher water
75 contents were obtained in steady state for the butanol solution than for water and attributed
76 this difference to the relatively higher viscosity of the butanol solution. Henry et al. [19]
77 studied the effect of solute solubility on unsaturated flow and concluded that the surfactants
78 can significantly affect the flow in unsaturated porous media. Through a series of closed,
79 horizontal sand column experiments, they demonstrated that the surfactant-induced flow
80 caused by a highly soluble compound such as butanol was very different from the flow caused
81 by a relatively insoluble surfactant such as myristyl alcohol, though both induced a similar
82 reduction in the surface tension of water. This difference was attributed to the fact that, unlike
83 butanol, myristyl alcohol is virtually insoluble and primarily resides at the air-water interface
84 rather than in the bulk solution. Thus, flow only occurs at surfactant concentrations that are
85 greater than or equal to those needed to completely cover the air-water interface, which leads
86 to an ineffective transport of myristyl alcohol to previously clean regions [23]. In another
87 study of surfactant-induced flow phenomena, Henry et al. [20] found that hysteresis was an
88 important factor in horizontal flow. They conducted experiments in closed, horizontal
89 columns filled with silica sand and with butanol as the surfactant. They also modified a one-
90 dimensional hysteretic unsaturated flow and transport numerical model to include the
91 dependence of surface tension and viscosity on concentration. Under hysteretic conditions and
92 at final steady state, the model predicted uniform concentration and pressure profiles, but a
93 non-uniform liquid content profile unlike the situation expected if the system was non-
94 hysteretic. Also, flow simulations were sensitive to dispersivity. As Henry et al. [20] noted,
95 lower dispersivity caused sharper surfactant concentration gradients, which led to larger
96 capillary pressure gradients and higher fluxes near a solute front. In the same context, these
97 authors [22] modified a two-dimensional model for flow and transport in unsaturated soils to

98 include the dependence of surface tension and viscosity on the surfactant concentration. They
99 directly compared the simulations to the sand box infiltration experiments with butanol-water
100 mixtures presented by Henry and Smith [21]. A longitudinal dispersivity value of 1 cm was
101 used in the simulations and shown to cause too much dispersion relative to the experimental
102 data at larger travel distances. In a recent review of the surfactant-induced flow phenomena in
103 the vadose zone, Henry and Smith [23] presented experimental evidence that surfactant-
104 induced flow effects can be significant when considered on the laboratory scale. These effects
105 may be due to surfactant modifications of moisture retention characteristics and unsaturated
106 hydraulic conductivity, which affect unsaturated flow and chemical transport. They also
107 recognized that more work is needed to better understand the potential impact of surfactant-
108 induced flow effects on field-scale transport in the vadose zone and suggest that models
109 should include a better description of processes and phenomena such as hysteresis in the
110 hydraulic functions, vapor-phase transport of surfactant or partitioning of surfactant to the
111 different phases.

112 Despite all of these studies, the effects of several common simplifications for modeling non-
113 passive transport of solutes have still not been evaluated. Although several numerical models
114 can be adapted to simulate some situations of non-passive transport through the vadose zone
115 in multiphase systems, e.g., STOMP [46] and VST2D [13], in most of them it is considered
116 that several properties are independent of the mixture composition.

117 In this paper, we present a model for non-passive infiltration-redistribution and transport of
118 water-soluble solutes in the vadose zone. This model incorporates the dependence of density,
119 viscosity, surface tension, molecular diffusion coefficient in the liquid phase, and the gas-
120 liquid and solid-liquid partition coefficients, on the solute concentration. We also include the
121 reduction in the gas-liquid partition coefficient due to high capillary pressures in accordance
122 with Kelvin's equation for multicomponent mixtures. The effects of these dependencies were

123 illustrated using a one-dimensional numerical implementation of the transport model to
 124 simulate the infiltration, redistribution and volatilization of alcohol-water mixtures into
 125 different soils.

126

127

128 **2. Basic equations and numerical resolution**

129

130 *2.1. Balance equations*

131

132 The unsaturated soil system considered consists of liquid (*l*), gas (*g*) and solid (*s*) phases.
 133 Components that may be present within these phases are water, dry-air and $N - 2$ water-
 134 soluble organic compounds. The mass-conservation equations for component k under
 135 isothermal conditions were described by [17]

136

$$137 \quad \frac{\partial \theta_l C_l^k}{\partial t} = -\nabla \cdot [\mathbf{J}_l^k + \mathbf{q}_l C_l^k] - a_{lg}^k N_{lg}^k - a_{ls}^k N_{ls}^k \quad (1a)$$

$$138 \quad \frac{\partial \theta_g C_g^k}{\partial t} = -\nabla \cdot [\mathbf{J}_g^k + \mathbf{q}_g C_g^k] + a_{lg}^k N_{lg}^k \quad (1b)$$

$$139 \quad \frac{\partial \theta_s C_s^k}{\partial t} = a_{ls}^k N_{ls}^k \quad (1c)$$

140

141 where C_i^k (kg/m³) is the concentration of component k ($k = 1, \dots, N$) in the phase i ($i = l, g, s$), θ_i
 142 (m³/m³) is the volumetric fraction of that phase, \mathbf{q}_i (m/s) is the i phase specific discharge, N_{ij}^k
 143 (kg/m² s) is the interface mass flux of component k from phase i to phase j , and a_{ij}^k (m²/m³) is
 144 the interfacial area between phases i and j by unit volume of porous matrix. The diffusive-
 145 dispersive mass flux vector \mathbf{J}_i^k (kg/m² s) is given by

146

147

$$J_i^k = -\theta_i D_i^k \nabla C_i^k \quad (2)$$

148

149 where D_i^k (m^2/s) is the diffusion-dispersion tensor for component k [4]. Under the assumption
150 of local phase equilibrium [17], the three component equations (1) can be combined to give

151

$$\frac{\partial \varphi_k C_l^k}{\partial t} = -\nabla \cdot (\mathbf{J}_l^k + \mathbf{J}_g^k + \beta_k C_l^k) \quad (3a)$$

153

$$\varphi_k = \theta_l + \theta_g H_{gl}^k + \theta_s H_{sl}^k \quad (3b)$$

154

$$\beta_k = q_l + q_g H_{gl}^k \quad (3c)$$

155

156 Assuming that dry-air is present neither in the liquid-phase nor in the solid-phase, only the
157 gas-phase transport (equation (1b)) was considered for the dry-air mass conservation equation

158

$$\frac{\partial \theta_g C_g^a}{\partial t} = -\nabla \cdot [\mathbf{J}_g^a + q_g C_g^a] \quad (4)$$

160

161 where C_g^a is the dry-air concentration in the gas-phase.

162 The specific discharge of phase i , q_i (m/s), is given by the generalized Darcy's law [4]

163

$$q_i = -\frac{k k_{ri}}{\mu_i} (\nabla P_i + \rho_i g z) \quad (5)$$

165

166 In equation (5), \mathbf{k} is the intrinsic permeability tensor of the soil (m^2), $g\mathbf{z}$ (m/s^2) is the gravity
 167 vector, k_{ri} is the relative permeability (dimensionless), ρ_i (kg/m^3) is the density, μ_i (kg/m s) is
 168 the dynamic viscosity, and P_i (Pa) is the pressure of phase i .

169 The diffusive-dispersive mass flux vector of air \mathbf{J}_g^a ($\text{kg/m}^2 \text{ s}$) was calculated from the
 170 condition

171

$$172 \quad \sum_{k=1}^N \mathbf{J}_g^k = 0 \quad (6)$$

173

174 The partition coefficient, H_{ij}^k , between phases i and j is defined by

175

$$176 \quad H_{ij}^k = \frac{C_i^k}{C_j^k} \quad i, j = g, l, s \quad (7)$$

177

178 Use of constant partition coefficients is a common assumption when modeling solute
 179 transport in variably-saturated soils. However, in this work the gas-liquid partition coefficient,
 180 H_{gl}^k , was assumed to be dependent on solute concentration and soil-liquid content [10, 11, 12]
 181 as given by

182

$$183 \quad H_{gl}^k = H_{gl}^{*k} \exp\left(\frac{P_M \hat{V}_k}{RT}\right) \quad (8)$$

184

185 where the exponential term accounts for the Kelvin's effect in multicomponent liquid
 186 mixtures [39, 42]. In (8), \hat{V}_k (m^3/mol) is the partial molar volume of component k in the
 187 liquid-phase, R is the universal gas constant, $P_M = P_l - P_g$ (Pa), is the matric pressure of the

188 liquid and T (K) is the temperature. The gas-liquid partition coefficient for plane interfacial
189 surfaces corresponds to the dimensionless Henry's law constant, H_{gl}^{*k} , and its dependence on
190 component concentration was calculated from the liquid-vapor equilibrium condition [45]

191

$$192 \quad H_{gl}^{*k} = \gamma_k \frac{p_{vap}^k \hat{V}_m}{RT} \quad (9)$$

193

194 in which p_{vap}^k (Pa) is the vapor pressure of component k , \hat{V}_m (m^3/mol) is the partial molar
195 volume of the liquid mixture, and γ_k (dimensionless) is the activity coefficient of component
196 k . In very dry soil conditions, the small quantity of liquid in the medium is no longer under
197 the influence of capillary forces so, strictly speaking, the original matric pressure definition is
198 not applicable. Nevertheless, as Baggio et al. [3] suggested, the matric pressure definition can
199 be expanded as

200

$$201 \quad P_M = -\frac{\Delta h}{\hat{V}_m} \quad (10)$$

202

203 where Δh (J/mol) refers to the enthalpy difference between the vapor in the gas-phase and the
204 condensed and/or adsorbed liquid-phase, excluding the latent enthalpy of vaporization.
205 Taking this definition, matric pressure and Kelvin's equation can be applied throughout all the
206 range from wet to dry conditions [15, 41].

207

208 *2.2. Boundary conditions, dispersivities and numerical procedure*

209

210 In this work, the one-dimensional version of the non-passive transport model described
 211 previously was implemented to simulate the infiltration, redistribution and
 212 volatilization/evaporation of alcohol-water mixtures in soils. A dynamic boundary condition
 213 at the surface was set to accommodate either a given infiltration or an
 214 evaporation/volatilization flux. In case of infiltration, the top boundary condition for the
 215 transport of each component (equation (3)) was the component mass flux at the surface, $N_o^{(k)}$
 216 ($\text{kg/m}^2 \text{ s}$), calculated as

217

$$218 \quad N_o^k = q_{lo} C_{l,in}^k \quad (11)$$

219

220 where q_{lo} (m/s) is the given infiltration liquid specific discharge and $C_{l,in}^k$ (kg/m^3) is the
 221 concentration of component k in the infiltrating liquid. In the absence of infiltration, the
 222 evaporation/volatilization mass flux for component k at the surface was calculated by
 223 considering a mass transfer limitation from the soil surface to the bulk atmosphere

224

$$225 \quad N_o^k = k_o^k (C_{bk}^k - C_{go}^k) \quad (12)$$

226

227 In equation (12), k_o^k (m/s) is the atmosphere-side mass transfer coefficient for component k ,
 228 C_{bk}^k (kg/m^3) is the background concentration of component k in the atmosphere, and C_{go}^k
 229 (kg/m^3) is the concentration of component k in the gas-phase at the soil surface. For given
 230 values of wind velocity, soil roughness and Schmidt number of the chemical volatilized, the
 231 mass transfer coefficients, k_o^k , were estimated with the semi-empirical correlation proposed
 232 by Brutsaert [8]. This correlation is only applicable under neutral atmospheric conditions and
 233 was developed from available experimental data. In case of non-neutral conditions a different

234 approach using the Obukhow length should be used as suggested by Brutsaert [8]. In all cases,
 235 the boundary condition at the bottom was set as zero diffusive and dispersive fluxes and zero
 236 matric pressure gradient. The lower gas-phase boundary condition was set as a no-flow
 237 boundary, while the upper gas-phase boundary condition was a constant atmospheric pressure.

238 The longitudinal diffusion-dispersion coefficient for component k , D_i^k (m²/s), was calculated
 239 as

240

$$241 \quad D_i^k = \frac{D_{oi}^k}{\tau_i} + D_{Li} \quad (13)$$

242

243 where the molecular diffusion and the longitudinal dispersion coefficients in phase i are
 244 denoted by D_{oi}^k (m²/s) and D_{Li} (m²/s), and τ_i (dimensionless) is the tortuosity of phase i .

245 Tortuosities, τ_g and τ_l , were evaluated according to the first model of Millington and Quirk
 246 [26], i.e. $\tau_i = \varepsilon^{2/3} / \theta_i$. Longitudinal dispersion coefficients for each phase were calculated as

247 $D_{Li} = \alpha_{Li} q_i / \theta_i$, where α_{Li} (m) is the longitudinal dispersivity for phase i given as a function of
 248 the volumetric phase content, in accordance with the correlation proposed by Grifoll et al.
 249 [18].

250

$$251 \quad \alpha_{Li} = \alpha_{Li}^0 (13.6 - 16S_i + 3.4S_i^5) \quad (14)$$

252

253 in which $S_i = \theta_i / \varepsilon$ is the actual saturation of phase i and α_{Li}^0 is the dispersivity at saturation.

254 Grifoll and Cohen [17] used a similar approach to equation (14). As they pointed out, the
 255 adoption of an empirical longitudinal dispersivity model, like described by equation (14), is

256 not meant to suggest its general applicability, but can be used to illustrate a general trend in
257 dispersivity behavior.

258 The governing partial differential equations, equations (3) and (4), were discretized spatially
259 and temporally in algebraic form using the finite volumes method [34] with a fully implicit
260 scheme (backward Euler) for time integration. The non-linear discretized governing equations
261 were solved using the multivariable Newton-Raphson iteration technique [26]. Volumetric
262 liquid content, dry-air concentration in the gas-phase and alcohol concentration in the liquid-
263 phase were selected as primary variables. The Jacobian coefficient matrix was calculated
264 using a finite difference approximation [26]. The linear system of equations formulated in the
265 Newton-Raphson method was solved for the correction to the primary variables by the
266 iterative Preconditioned Biconjugate Gradient Method [26, 35]. The preconditioner matrix
267 was the diagonal part of the Jacobian coefficient matrix [35]. Values for the convergence limit
268 and maximum number of Newton-Raphson iterations have been defined conveniently as input
269 parameters. Convergence limits were defined with respect to the maximum residual of each
270 mass balance equation, normalized by the sum of the mass fluxes absolute values. The
271 tolerance employed in all simulations was 10^{-7} while the maximum number of Newton-
272 Raphson iterations was set to 10. If the convergence limit was not satisfied after 10 iterations,
273 the time step was reduced to 50% and the calculation was restarted from the end of the
274 previous time step. Otherwise, if the convergence was attained within the maximum number
275 of iterations, the time step was doubled without exceeding a maximum $\Delta t_{max} = 60$ s, and a
276 new time step was initiated.

277 The one-dimensional grid was generated by distinguishing two regions. First, from the
278 surface to a depth of $z = 0.135$ m and starting with $\Delta z_1 = 0.2$ mm, the grid spacing increases
279 with a progression factor of 1.008. Second, from $z = 0.135$ m to the bottom of the system
280 ($z = 0.5$ m) the grid was set uniform with a grid spacing of $\Delta z = 1.33$ mm.

281 The sensitivity of the numerical solution to grid spacing and time step was analyzed for Test
282 Case I as it is described in section 3.2.1 below. For the standard grid and maximum time step
283 given above, maximum discrepancies between the numerical results and the exact values are
284 expected to be less than 1%.

285 To check the numerical algorithm, we compared the solution of the passive transport of
286 water-methanol mixtures into a loam-type soil with the solution reported by Grifoll and
287 Cohen [17]. The maximum discrepancy between these two solutions was also less than 1%.

288

289

290 **3. Results and discussion**

291

292 The present numerical model has been used to simulate several test cases in order to
293 investigate the non-passive transport behavior of volatile organic compounds. The first test
294 presented is the infiltration of water-butanol mixtures into sand as reported by Smith and
295 Gillham [44]. Their experimental and simulation results were compared to the present
296 numerical results in order to check our model, the numerical algorithm and the computational
297 code. The next two test cases were for the infiltration of methanol-water mixtures into a
298 Sandy Clay Loam and Silty Clay soils. These test cases illustrated how the dependency of
299 physical properties on concentration affects a system in which the solute is soluble in water at
300 any proportion. Initial test simulations showed that the convective gas-phase component did
301 not contribute effectively to the transport of methanol and water. In the present test cases of
302 soils with relatively low permeabilities, the inclusion of gas-phase convection did not change
303 the evolution of the volumetric liquid content and methanol concentration profiles by more
304 than 0.5% and very high CPU times were required. Note that the differences in gas-phase
305 densities due to the saturation or absence of methanol were not high enough to induce density-

306 dependent advection [28]. In addition, as stated by Lenhard et al. [28], effects of density-
307 driven vapor flow are more evident in porous media with permeabilities greater than 10^{-11} m^2 .
308 On the contrary, the permeabilities of the soils studied in this work are less than $4 \times 10^{-13} \text{ m}^2$.
309 Most of the results presented in the next sections were therefore obtained by neglecting gas-
310 phase convection when solving the numerical model.

311

312 *3.1. Dissolved butanol infiltration*

313

314 Smith and Gillham [44] studied the infiltration of a butanol-water mixture into a 2 meters
315 column-sand. Their experimental procedure consisted of infiltrating distilled water until the
316 steady state was reached and then changing the infiltration liquid to an aqueous solution of
317 butanol with 7% w/w at the same infiltration rate. Their experimental results were compared
318 with their earlier numerical transport model [43], which was modified to include the
319 dependencies of surface tension and viscosity on butanol concentration. Figure 1 shows the
320 evolution of the pressure head and liquid content measured at a depth of 38 cm in the column,
321 the simulation results of Smith and Gillham [44], and the present numerical calculations. For
322 the present simulation, the dependency of surface tension and viscosity on solute
323 concentration, as well as the soil water retention curve, were taken from Smith and Gillham
324 [44]. A measured constant dispersivity $\alpha_{Li} = 0.00177 \text{ m}$ [44] was also used in this case.

325 Deviations from steady state in pressure head and liquid content after the application of
326 butanol solution were observed. These variations were due to the dependency of surface
327 tension and viscosity on butanol concentration.

328 As the solute front passed, the water content significantly decreased to a minimum before
329 increasing to a slightly higher value than that of the previous steady state. The highly

330 localized drainage and rewetting were caused by hydraulic gradients induced by the surface
331 tension variations associated with the solute front.

332 Both the model of Smith and Gillham [44] and the present model describe the main
333 characteristics of the experiment. It should be noted that the model parameters used by Smith
334 and Gillham [44] were estimated independently of the experimental results that appear in
335 Figure 1. They suggested that some experimental uncertainty could be introduced in the
336 measurement of dispersivity because it was determined using a concentrated solution of NaCl
337 that could be subject to density effects. Moreover, the differences in the pressure head and
338 volumetric liquid content between the two simulation results were less than 4.8%, which
339 gives an indication of the ability of the present model to simulate non-passive transport of
340 solutes.

341

342 *3.2. Methanol infiltration*

343

344 The impact of the non-passive behavior on the infiltration and redistribution of methanol-
345 water mixtures is illustrated in two cases in which different soils were used. In both of these
346 test cases we simulated a hypothetical scenario composed by an initial period of infiltration
347 followed by a period of volatilization/evaporation. Therefore, at least close to the soil surface
348 where volatilization and evaporation occur, the soil was expected to reach conditions of very
349 low liquid content ($\theta_l < 0.10$). To simulate these situations realistically, we used an extended
350 version of the Brooks-Corey soil water retention curve proposed by Rossi and Nimmo [38],
351 which is given as

352

$$353 \quad P_{M,w}(S) = \begin{cases} P_d e^{-S/\alpha_{RN}} & 0 \leq S < S_j \\ P_b S_e^{-1/\lambda} & S_j \leq S \leq 1 \end{cases} \quad (15)$$

354

355 In equation (15) $S = \theta/\varepsilon$ and $S_e = (S - S_r)/(1 - S_r)$ are the actual and effective liquid
356 saturation, respectively, $P_{M,w}$ (Pa) is the matric water pressure, while P_b (Pa) (bubble pressure
357 or air entry pressure), λ (pore size distribution index), and θ_r (residual volumetric water
358 content) are the classical Brooks-Corey parameters. The oven dry matric water pressure, P_d ,
359 was taken as 980 MPa, as suggested by Rossi and Nimmo [38]. The parameters α_{RN} and θ_j
360 ($S_j = \theta_j/\varepsilon$), introduced by these authors, were calculated as functions of the classical Brooks-
361 Corey parameters, as suggested by Morel-Seytoux and Nimmo [31]. Liquid-phase relative
362 permeability was computed as a function of liquid saturation from the soil-moisture retention
363 function according to the model of Burdine [9]

364

$$365 \quad k_{rl} = S^2 \frac{I(S)}{I(1)} \quad (16)$$

366 where

$$367 \quad I(S) = \begin{cases} \frac{\alpha}{2P_d^2} (e^{2S/\alpha_{RN}} - 1) & 0 \leq S < S_j \\ \frac{\alpha}{2P_d^2} (e^{2S_j/\alpha_{RN}} - 1) + \frac{\lambda}{\lambda + 2} \frac{(1 - S_r)}{P_b^2} (S_e^{1+2/\lambda} - S_{ej}^{1+2/\lambda}) & S_j \leq S \leq 1 \end{cases} \quad (17)$$

368

369 Given a volumetric liquid content, the matric pressure for pure water as given by equation
370 (15) has been scaled for mixtures with the methanol concentration C_l as [29]

371

$$372 \quad P_M = \frac{\sigma(C_l)}{\sigma_w} P_{M,w} \quad (18)$$

373

374 where σ_w is the surface tension of water and $\sigma(C_l)$ (N/m) is the surface tension of the liquid
375 mixture.

376 The physical properties of methanol-water mixtures depend on methanol concentration. In
377 this work, each of these dependencies has been described by a polynomial function, as

378

$$379 \quad p(C_l) = \sum_j a_j (C_l)^j \quad (19)$$

380

381 where p stands for any of the properties allowed to vary with methanol concentration (surface
382 tension, density, viscosity and diffusion coefficient of methanol in the liquid-phase) and C_l is
383 the methanol concentration in the liquid-phase. The polynomial coefficients a_j , obtained by
384 fitting equation (19) to available experimental data [14], are given in Table 1. Diffusion
385 coefficients of methanol and water in the gas-phase were taken as constants, with values
386 $D_{og}^m = 1.6 \times 10^{-5} \text{ m}^2/\text{s}$ [17] and $D_{og}^w = 2.6 \times 10^{-5} \text{ m}^2/\text{s}$ [37], respectively.

387 To calculate the gas-liquid partition coefficients for methanol and water, the partial molar
388 volumes and the activity coefficients according to equations (8) and (9) are required. Activity
389 coefficients for water and methanol were calculated using Wilson's equation [27] with the
390 parameters fitted by Gmehling et al. [16] to available experimental data. Molar volumes were
391 calculated following the procedure described by Lide and Kihiaian [30], who suggested the
392 Redlich-Kister equation to calculate molar excess volumes. The gas-liquid partition
393 coefficients H_{gl}^* for water and methanol calculated by this procedure are shown in Figure 2.
394 For water, this partition coefficient increases monotonically from 1.73×10^{-5} , in absence of
395 methanol, to the limiting value 6.14×10^{-5} as the pure methanol condition is approached. The
396 partition coefficient for methanol reaches a minimum value of 1.61×10^{-4} when $C_l = 405 \text{ kg/m}^3$
397 and then increases progressively to 2.17×10^{-4} , which is the value for pure methanol. Sorption

398 of methanol onto the soil solid was assumed to be described by a constant partition coefficient
399 $H_{sl}^m = 3.7 \times 10^{-3}$, estimated for a soil with 2% of organic matter [17]. In their experimental
400 work, Smith and Gillham [44] used homogeneous sand and therefore found low values of
401 dispersivity. In heterogeneous natural soils higher dispersivities are expected. Jaynes [24], for
402 instance, obtained values of dispersivity between 0.0453 and 0.25 m for a depth of 0.3 m.
403 Also, Abbasi et al. [1] estimated soil hydraulic and solute transport parameters from several
404 two-dimensional furrow irrigation experiments and obtained values of longitudinal
405 dispersivity between 0.026 and 0.328 m for a depth of 1 m. In this paper, dispersivity at
406 saturation for both the liquid and the gas phases was set to $\alpha_{Li}^o = 0.078$ m, the value suggested
407 by Biggar and Nielsen [5] for saturated soil conditions in an agricultural field [32]. In their
408 work, Biggar and Nielsen measured dispersivities in ponded soils (of a broad textural class:
409 loam, clay loam, silty clay, silty clay loam) under steady state infiltration conditions at depths
410 between 30.5 and 182.9 cm, infiltration pore velocities between 1.3 and 105.4 cm/day, while
411 hydraulic conductivities at saturation ranged from 0.3 to 70 cm/day. In the test cases of the
412 present work, the selected soils and process conditions were, most of the time, within the
413 range of values above described.

414

415 3.2.1. Test case I

416 The first case study involved five simulations of the infiltration of methanol-water mixtures
417 into a homogeneous Sandy Clay Loam soil, each with different methanol concentration of the
418 infiltrating liquid, $C_{l,in}$. These concentrations ranged from $C_{l,in} = 0.001$ kg/m³, in which the
419 methanol behaves as a passive scalar, to $C_{l,in} = 786.6$ kg/m³, which corresponds to pure
420 methanol. The upper boundary condition was set at an infiltration rate of 0.25 cm/hr for 15
421 hours, followed by 57 hours in which the methanol and water were allowed to volatilize at the
422 surface according to equation (12). The background concentration of methanol in the

423 atmosphere was assumed to be zero, while the background concentration of water in the
424 atmosphere was calculated assuming a relative humidity of 40%. The initial condition was a
425 uniform volumetric water content of $0.128 \text{ m}^3/\text{m}^3$, which corresponds to a matric potential of
426 -100 m . The hydraulic parameters of equations (15), (16) and (17), taken from Rawls and
427 Brakensiek [36] as typical values for a Sandy Clay Loam soil, are given in Table 2.

428 When comparing the results of the simulations for different grid spacing and time steps, it is
429 observed that methanol concentration and volumetric liquid content values at the surface are
430 the most sensitive to these variations. Five simulations with different grid spacing were run
431 for a maximum time step of $\Delta t_{max} = 60 \text{ s}$ and $C_{l,in} = 400 \text{ kg/m}^3$. A coarse grid with $N = 125$
432 control volumes was used in the first simulation. In the following ones, the number of control
433 volumes N was successively doubled by halving the grid spacing. The methanol concentration
434 and the volumetric liquid content at the surface at the end of the simulations were extrapolated
435 to an infinite number of volumes, C_{l0}^∞ and θ_{l0}^∞ . Figure 3(a) shows the ratio of C_{l0} and θ_{l0} to
436 their extrapolated value C_{l0}^∞ and θ_{l0}^∞ as a function of the inverse of the number of control
437 volumes. Deviations from the extrapolated value were higher in the case of methanol
438 concentration. However, for both concentration and volumetric liquid content, and for all
439 grids tested, the relative deviations were less than 0.6%. The sensitivity of simulations to time
440 step was tested using the grid described at the end of section 2.2 (500 volumes) and
441 $C_{l,in} = 400 \text{ kg/m}^3$. Five simulations were run with $\Delta t_{max} = 240, 120, 60, 30$ and 15 s and the
442 values at the surface extrapolated to zero time step. Figure 3(b) shows that methanol
443 concentration at the surface was sensitive to time step, although for $\Delta t_{max} < 240 \text{ s}$, the
444 concentration differences respect the extrapolated value were less than 5%. For the standard
445 simulation conditions ($N = 500, \Delta t_{max} = 60 \text{ s}$), the maximum deviations expected are less than
446 1%.

447 Figure 4 shows the volumetric liquid content and normalized concentration profiles 48 hours
448 after the beginning of the experiment for five methanol concentrations in the infiltrating
449 liquid. Normalization has been carried out with respect $C_{l,in}$ in order to emphasize the
450 non-passive behavior because, in the case of passive transport, the normalized concentration
451 profiles in Fig. 4 should be independent of concentration since the solute transport equation
452 (3) is linear when the coefficients do not depend on the solute concentration.

453 The differences in volumetric liquid content profiles for different $C_{l,in}$, shown in Fig. 4(a),
454 are due to three factors: i) the dilution effect on the incoming mixture caused by the initial
455 pure water in the soil, ii) differences in the liquid-phase flow caused by changes in viscosity,
456 density and surface tension, and iii) the volatilization of the mixture. Note that the relative
457 densities of the mixture change from 1 for pure water to 0.786 for pure methanol. Then, when
458 methanol dilutes in water, the volume of the mixture should shrink due to the non-ideal
459 mixing effects as described by the dependence of density on concentrations (Eq. (19) and
460 Table 1). This effect is more pronounced when the infiltrating mixture is more concentrated in
461 methanol. During infiltration the causes of the differences in volumetric liquid content are this
462 non-ideal mixing effect and the changes in liquid flow caused by variations in viscosity and
463 surface tension. In the case of pure methanol and after 48 hours of simulation (i.e. 33 hours of
464 volatilization), by balancing the volumes of initial water, infiltrated liquid, final liquid in the
465 soil and volatilized liquid, it was calculated that the non-ideal mixing effect is about 3.6% of
466 the initial water plus infiltrated liquid volume, whereas the percentage of volatilized liquid is
467 about 9.6%. The relative influence of changes in liquid flow due to variations in viscosity and
468 surface tension cannot be deduced from this balance, but the percentage of volatilized liquid
469 increases from 5% of the initial plus infiltrated volume for pure water, to a maximum of 10%
470 at a concentration of $C_{l,in} = 400 \text{ kg/m}^3$, and then decreases to 9.6% for pure methanol. Note
471 that the viscosity of the liquid is a concave function of the methanol concentration, reaching a

472 maximum at about 392 kg/m^3 . This shows that more viscous infiltrating mixtures move more
473 slowly and consequently, by remaining close to the surface for a longer period, undergo a
474 higher volatilization. Because of the combined effect of volatilization, viscosity and surface
475 tension dependent flow, and non-ideal mixing, the front position for passive transport
476 ($C_{l,\text{in}} = 0.001 \text{ kg/m}^3$) is 29.4% deeper than for pure methanol ($z = 0.34 \text{ m}$). Moreover, the
477 liquid content near the surface also depends on $C_{l,\text{in}}$ because, as is explained below, the
478 volatilization rate at the surface is low for low concentrations of methanol.

479 The gas-liquid partition coefficient for methanol is between 6 and 10 times higher than for
480 water (see Fig. 2). Higher overall volatilization rates are therefore observed for more
481 concentrated mixtures. The differences in the normalized methanol concentration profiles
482 developed at the soil top (Fig. 4(b)) are largely due to methanol transfer limitations from
483 inside the soil to the surface, which are higher for more dilute mixtures. This is shown in
484 Figure 4(b), where we find progressively larger differences between the concentration profiles
485 established in the first 10 cm adjacent to the soil surface, especially for $C_{l,\text{in}} > 400 \text{ kg/m}^3$.

486 The volatilization flux of methanol N_o^m , normalized by the corresponding flux at the
487 beginning of volatilization $N_{o,\text{ini}}^m$, is shown in Figure 5(a) for the five numerical experiments.
488 Volatilization decreases as the methanol concentration and liquid content at surface decrease.
489 These volatilization fluxes suffer a sudden decrease due to the development of high capillary
490 pressures near the surface, which reduce the gas-liquid partition coefficient according to the
491 exponential term in equation (8) (Kelvin effect). This behavior is similar to the decrease in
492 soil water evaporation rates from stage-one to stage-two evaporation [40]. At high infiltration
493 methanol concentrations, volatilization rates are higher. This leads sooner to these high
494 capillary pressures and, therefore, to the observed decrease in the volatilization flux.

495 The evaporation flux of water N_o^w undergoes a similar sudden regime change. However, as
 496 shown in Figure 5(b), after the infiltration has ceased the water evaporation rate increases due
 497 to the loss of methanol to the atmosphere, which increases the concentration of water at the
 498 soil surface. This initial period of increasing evaporation lasts until Kelvin's effect begins to
 499 be noticeable. During this first stage, normalized evaporation is higher at higher infiltrating
 500 methanol concentrations. Similar behavior in the time variation of the evaporation flux of
 501 water was experimentally and numerically observed by Chen et al. [11]. It is worth noting that
 502 when the Kelvin equation and the water vapor diffusion were not included in their water
 503 transport model, the simulation results deviated from the experimental measurements.

504 The role of the various contributions to total liquid movement can be illustrated by
 505 inspecting the individual partial fluxes due to capillary component and gravitational
 506 component. The partial fluxes can be defined, according to equation (5), as given below

507

$$508 \quad q_{l,cap} = -\frac{kk_{rl}}{\mu_l} \frac{\partial P_l}{\partial z} \quad (20a)$$

$$509 \quad q_{l,grav} = \frac{kk_{rl}}{\mu_l} \rho_l g \quad (20b)$$

510

511 where $q_{l,cap}$ and $q_{l,grav}$ are the capillary and gravitational components of the flux, respectively.

512 The contribution made by each of these components to the specific discharge after 48 hours
 513 of simulation and for each infiltration concentration is shown in Figure 6. For all cases, the
 514 contribution from the gravity flux was negligible and the main contribution was from
 515 capillary flux. There were significant differences in the capillary liquid flux due to the relative
 516 differences in dryness at the surface and the different viscosity profiles from different
 517 compositions of the infiltrating methanol-water mixture. Note that, for $C_{l,in} \geq 400 \text{ kg/m}^3$ and

518 close to the surface, the liquid flux drops to almost zero because of the low liquid content in
 519 this zone (see Fig. 4(a)), which makes the relative permeability negligible. On the other hand,
 520 the matric pressure depends on both the liquid content and the solute concentration. We can
 521 therefore divide the capillary flux into two components—one that is due to changes in
 522 volumetric liquid content and one to changes in the composition of the liquid mixture. These
 523 components are defined as

524

$$525 \quad q_{l,cap}^C = -\frac{kk_{rl}}{\mu_l} \frac{\partial P_l}{\partial C_l} \frac{\partial C_l}{\partial z} \quad (21a)$$

$$526 \quad q_{l,cap}^\theta = -\frac{kk_{rl}}{\mu_l} \frac{\partial P_l}{\partial \theta_l} \frac{\partial \theta_l}{\partial z} \quad (21b)$$

527

528 where $q_{l,cap}^C$ is the capillary liquid flux due to changes in methanol concentration and $q_{l,cap}^\theta$ is
 529 the corresponding flux due to variations in the liquid content. Figure 7 shows the
 530 contributions of these components for $C_{l,in} = 400 \text{ kg/m}^3$ after 48 hours of simulation. We can
 531 see that $q_{l,cap}^\theta$ is the main component of the capillary flux and that there is a small contribution
 532 of $q_{l,cap}^C$ from $z = 0.15 \text{ m}$ to the front position. Similar contribution profiles were obtained for
 533 the other $C_{l,in}$ cases, which indicates that, in the cases we studied, the main flow mechanism
 534 for the infiltration of methanol was the capillary component due to variations in liquid
 535 content.

536 The relative magnitude of the various mechanisms involved in the component transport
 537 through the soil can be illustrated by inspecting the individual partial fluxes due to diffusion,
 538 dispersion and convection. These partial fluxes are defined for each phase $i = l, g$ and each
 539 component k as

540

541
$$J_{dif,i}^k = -\theta_i \frac{D_{oi}^k}{\tau_i} \frac{\partial C_i^k}{\partial z} \quad (22a)$$

542
$$J_{disp,i}^k = -\theta_i D_{Li} \frac{\partial C_i^k}{\partial z} \quad (22b)$$

543
$$J_{conv,i}^k = q_i C_i^k \quad (22c)$$

544

545 Methanol and water transport by diffusion in the liquid-phase was negligible in all cases.
 546 Figure 8 shows the partial fluxes profiles for methanol and all the relevant mechanisms after
 547 48 hours of simulation since the start of the numerical experiment. These mechanisms are
 548 diffusion in the gas-phase, $J_{dif,g}^m$, and dispersion, $J_{disp,l}^m$, and convection, $J_{conv,l}^m$, in the liquid-
 549 phase. All the fluxes were normalized with respect to the volatilization flux at that time, N_o^m .
 550 Diffusion in the gas-phase is not an active mechanism for methanol transport, as we can see in
 551 Fig. 8(a), except very close to the surface and when $C_{l,in} \geq 400 \text{ kg/m}^3$. In these circumstances
 552 the soil close to the surface is very dry (see Fig. 4(a)) and in this region no mechanism in the
 553 liquid-phase is able to transport the methanol. Diffusion in the gas-phase is therefore the only
 554 active mechanism in this thin region. The methanol concentration gradient that drives the gas-
 555 phase diffusion is magnified by the Kelvin effect that decreases the concentration of methanol
 556 close to the surface, as the soil becomes drier. Numerical experiments with higher $C_{l,in}$ causes
 557 a decrease in the liquid saturation which induce higher gas-phase diffusive fluxes. For
 558 $C_{l,in} < 400 \text{ kg/m}^3$, the top soil is not so dry because volatilization is lower for lower
 559 concentrations of methanol. For these low input concentrations, therefore, dispersion in the
 560 liquid-phase (see Fig. 8(b)) is the most active mechanism, and accounts for 90% of the
 561 transport at the surface.

562 It is important to note the close relationship between the volumetric liquid content and
 563 concentration profiles in Fig. 4, the liquid-phase velocities in Fig. 6 and the partial mass

564 fluxes in Fig. 8. For example, at the depth corresponding to the liquid front position for the
565 various cases viscosity increases as the infiltrating mixture becomes more concentrated. As
566 the viscosity is higher, the velocities are lower and a decrease in dispersion in the liquid-phase
567 could be expected. However, the higher the infiltrating concentration, the lower the liquid
568 volumetric content and the higher the methanol concentration gradients. This leads to higher
569 partial dispersive fluxes (equation (22b)) in this zone for more concentrated infiltrating
570 mixtures (see Fig. 8(b)). A similar analysis explains the interaction between the liquid-phase
571 velocity, the different transport mechanisms and the liquid content and concentration profiles
572 in the upper part of the soil ($z \leq 0.15$ m).

573 Results of the simulations previously described appear to be inconsistent with experimental
574 and modeling observations of Smith and Gillham [44]. Unlike our simulations that predict a
575 main flow mechanism driven by the capillary component due to variations in liquid content
576 (see Fig. 7), Smith and Gillham [44] observed a significant impact of the solute concentration
577 on unsaturated flow. This discrepancy in principle may be due to our use of a large
578 dispersivity value that reduces the concentration gradient and thereby reduces the magnitude
579 of the effect of the solute on unsaturated liquid fluxes. However, it should be noted that the
580 increase in the matric pressure due to the reduction of the surface tension in accordance with
581 the scaling proposed by Leverett [29] is more pronounced in case of butanol aqueous solution
582 than with aqueous mixtures of methanol. As explained by Smith and Gillham [43] *“butanol,*
583 *0-7% by weight at 25 °C, causes a nonlinear and relatively large change in surface tension*
584 *with concentration. Methanol, 0-7% by weight at 25 °C, causes a near linear and relatively*
585 *small change in surface tension”*. A simple calculus shows that in the case of butanol the
586 reduction is about 70% in the range of 0-7% by weight. Here it is noteworthy that
587 experiments and simulations carried out by Smith and Gillham [43, 44] involve scenarios of
588 pure infiltration, unlike our simulations, which include infiltration followed by the

589 volatilization of the mixture. For aqueous solutions of methanol and in the full range of
590 solubility the reduction in surface tension is also 70%. Nevertheless, during volatilization and
591 $C_{l,in} = 400 \text{ kg/m}^3$, the concentration of methanol within the soil is reduced to less than 40% of
592 this inlet composition, which involves a surface tension reduction of 32%. In order to
593 demonstrate the sensitivity of the results to dispersion, the Test Case I simulations were
594 repeated with a dispersivity value of 0.2 cm. As shown in Figure 9, the variability in
595 concentration profiles diminished compared to the 7.8 cm dispersivity results, while the
596 differences in volumetric content near the top prevailed due to volatilization. As expected,
597 with a dispersivity of 0.2 cm the solute front is not so dispersed as with 7.8 cm (Fig. 9(b)).
598 Indeed, for a dispersivity of 0.2 cm the solute front is located at a depth that is the half of the
599 liquid front position. An additional observation is that the volumetric liquid content shows a
600 notch just in the solute front position. This notch was not so evident for a dispersivity of 7.8
601 cm (Fig. 4(a)), but with a dispersivity of 0.2 cm it grows, especially for the more concentrated
602 mixtures. A similar notch was observed by Allred and Brown [2] in their experiments who
603 concluded that it is caused by a modification in the soil-water retention relationship in the
604 transition zone of the soil between high and low concentrations. Figure 10 shows the capillary
605 liquid flux and its components for a dispersivity value of 0.2 cm. We can see that now, for
606 $C_{l,in} = 400 \text{ kg/m}^3$ and at $t = 48$ hours (during volatilization), the capillary liquid flux due to
607 changes in the composition is the predominant mechanism of liquid flow in the region
608 delimiting the solute front. The sensitivity analysis of the model to dispersion demonstrates
609 that, for aqueous mixtures of methanol and low dispersivities, changes in surface tension due
610 to variation in composition may induce important liquid flow. This result agrees with
611 simulations and experimental results obtained by other authors [20, 21, 22, 44].

612 The coupled non-passive transport of liquid and a solute through the unsaturated zone is
613 therefore a highly interactive phenomenon in which matric pressure gradients can induce

614 solute transport and, reciprocally, mixture composition may change the transport properties
615 and induce a flow pattern.

616

617 3.2.2. *Test case II*

618 A second case study was carried out to illustrate the potential impact of the Kelvin effect on
619 non-passive transport of solute in the vadose zone and its impact on the volatilization of
620 methanol and the evaporation of water. In some simulations in this case study, the Kelvin
621 exponential factor of equation (8) was not considered except at the surface, and the results
622 were compared to simulations in which full consideration of this factor along the system was
623 taken into account. Note that, if the methanol-water mixture is allowed to volatilize/evaporate
624 at a rate that is independent of the liquid content at surface, i.e. ignoring the Kelvin factor, no
625 decrease in volatilization/evaporation fluxes would be observed and a regime like stage-two
626 evaporation [40] would not be attained. With a stage-one like volatilization/evaporation
627 remaining indefinitely, the system would progress to a non-feasible physical situation in
628 which there would be no mechanism for the transport of components from the inside to the
629 soil surface able to maintain these relatively high volatilization/evaporation fluxes dictated by
630 the atmosphere-side mass transfer limitations. In all present simulations, therefore, the Kelvin
631 effect at the surface was considered in order to attain feasible physical situations.

632 The simulations for this second case were the infiltration and redistribution of a methanol-
633 water mixture into a Silty Clay soil. The infiltrating methanol concentration was $C_{l,in} = 400$
634 kg/m^3 and the infiltration rate was set at 0.075 cm/hr for 20 hours, followed by 148 hours in
635 which the methanol and water were allowed to redistribute and volatilize. Like in the Test
636 Case I we assumed the background concentration of methanol to be zero, and calculated the
637 background concentration of water in the atmosphere assuming a relative humidity of 40%.
638 The hydraulic parameters of a typical Silty Clay soil were selected as given by Rawls and

639 Brakensiek [36] and listed in Table 2. The hydraulic characteristic of this soil allows high
640 capillary pressures to develop at a relatively high liquid content, a condition for which we
641 expect the Kelvin effect to have a greater impact. The initial condition for the simulation was
642 a constant volumetric water content of $0.169 \text{ m}^3/\text{m}^3$, which corresponds to a matric head of
643 -500 m .

644 Figure 11 shows the liquid content and normalized concentration profiles 48 and 168 hours
645 after the start of the simulation (28 and 148 hours of volatilization/evaporation, respectively).
646 The dotted line represents the results obtained when the Kelvin effect within the soil is
647 ignored. At both 48 and 168 hours, and along the first 5 cm, the volumetric liquid content is
648 lower when the Kelvin factor is allowed to act within the soil. As Fig. 11(a) shows, this
649 difference increases with time as the soil dries. The maximum difference in the volumetric
650 liquid content is located within the first 5 cm adjacent to the soil surface, increasing from
651 122.4% after 48 hours to 129.8% after 168 hours. For the normalized methanol concentration
652 this difference increases from 32.8% after 48 hours to 42.8% after 168 hours.

653 To evaluate the impact of including the Kelvin effect in simulations, it is important to note
654 that the main transport mechanism affected is diffusion in the gas-phase. This can easily be
655 deduced from the definition of gas-liquid partition coefficient and equation (22). At this point
656 it is helpful to analyze the case of the transport of pure water. In that case, the vapor
657 concentration gradients within the soil are only those developed due to the reduction of the
658 vapor pressure according to the Kelvin equation. Consequently, the diffusion of water in the
659 gas-phase disappears if the Kelvin reduction factor is ignored within the soil and, therefore,
660 the soil dries slower than when Kelvin effect is considered within the soil. In fact, ignoring or
661 including the Kelvin effect within the soil is equivalent to consider or neglect the transport of
662 water by gas-phase diffusion. This problem was studied by Chen et al. [11], who found that
663 including the contribution of water vapor diffusion in water transport is important for

664 improving the accuracy of water content and water flux prediction. It is noteworthy that these
665 authors obtained differences in water content profile near the soil surface predicted when
666 water vapor diffusion was and was not included in the water transport simulations, which are
667 similar to the differences in volumetric liquid content shown in Fig.11(a) caused by including
668 or ignoring the Kelvin effect within the soil. The impact of Kelvin effect on the gas-phase
669 diffusion fluxes of methanol and water are shown in Figure 12. These fluxes have been
670 normalized by the respective fluxes of volatilization and evaporation at the beginning of the
671 volatilization period (20 h). As we can see in Fig. 12, gas-phase diffusion is significantly
672 reduced when Kelvin effect is ignored in the model. If the Kelvin effect is considered over the
673 entire soil, the drying process near the surface significantly reduces the liquid-phase flux and,
674 therefore, the liquid-phase convection and dispersion. This reduction in dispersion in the
675 liquid-phase along the first 2 cm is compensated by an increase in gas-phase diffusion in this
676 region. When the Kelvin effect is allowed to act only at the surface, the concentration in the
677 gas-phase within the soil is not affected by matric pressure variations and the changes in
678 concentration in the liquid-phase are insufficient to increase the gas-phase diffusion. As in
679 this situation the liquid content is higher under relatively steep liquid concentration gradients,
680 there are relatively high liquid-phase dispersive fluxes that at least partially compensate for
681 the incapability of the gas-phase diffusion transport. The Kelvin effect also affected, in a
682 similar way, the transport of water by dispersion in the liquid-phase and gas-phase diffusion.

683 Due to the low gas-phase diffusion of both methanol and water when the Kelvin effect is
684 ignored within the soil, volatilization and evaporation rates are lower than the respective
685 fluxes obtained when the Kelvin factor is considered within the soil. This situation is
686 illustrated in Fig. 13, which shows the evolution of the methanol volatilization and water
687 evaporation at the surface. We can see that there is a small difference in the volatilization flux
688 of methanol but a significant one in the evaporation flux of water. Under certain conditions

689 (clay and dry soil), therefore, there may be a great difference between considering the Kelvin
690 effect within the soil and ignoring it. This difference is reflected in the fluxes for transport to
691 the surface and mainly affects the less volatile compound (water, in this case).

692 We can conclude from this case study that the Kelvin effect plays an important role in
693 properly representing the dynamic behavior of solute volatilization and water evaporation
694 under high capillary pressures.

695

696

697 **4. Conclusions**

698

699 A model for the non-passive infiltration, redistribution and volatilization of liquid mixtures
700 has been developed. It has been used to illustrate the transport of butanol and methanol
701 aqueous solutions in the vadose zone. The coupled non-passive transport of liquid and solute
702 through the unsaturated zone is a highly interactive phenomenon. Matric pressure gradients
703 can induce solute transport. Reciprocally, the mixture composition may change the transport
704 properties and induce a given pattern of flow.

705 Simulations for completely miscible methanol-water mixtures and two different soils (Sandy
706 Clay Loam and Silty Clay) showed significant differences in volatilization fluxes, front
707 position, liquid content and concentration profiles that depend on the composition of the
708 infiltrating liquid. For the cases we studied and a dispersivity value of 7.8 cm, the
709 predominant mechanism in the transport of methanol through the soil was dispersion in the
710 liquid-phase, with a major contribution from gas-phase diffusion near the surface during
711 volatilization. By decomposing the liquid flux into capillary and gravity components, we
712 found that the liquid flow is mainly due to pressure gradients induced by changes in the
713 volumetric liquid content. However, simulations with a lower dispersivity (0.2 cm) showed

714 that, in this case, convection was more active for methanol transport than dispersion. Also in
715 this case, the capillary liquid flux due to changes in the composition is the predominant
716 mechanism of liquid flow in the solute-front region.

717 Including or ignoring in the model the reduction of gas-liquid partition coefficients
718 according to the Kelvin equation has an important impact on the global transport behavior.
719 When the Kelvin effect was ignored within the soil, the gas-phase diffusion was significantly
720 lower. The corresponding evaporation flux of water was also lower and, therefore, the
721 volumetric liquid contents were greater. The maximum differences in the volumetric liquid
722 content and normalized methanol concentration profiles were developed in the first 5 cm
723 adjacent to the soil surface. These differences were increasing with time, reaching the values
724 of 130 % and 43 % respectively at the end of the simulation. It was found that, under dry
725 conditions on a Silty Clay soil, mass fluxes that transport the solute to the surface can be
726 significantly different when the Kelvin factor is considered within the soil from when it is
727 ignored. This directly affects the dynamic of solute volatilization and water evaporation rates.
728 This phenomenon may play an important role under conditions of severe dryness, which
729 could be crucial to accurately model the fluid flow and contaminant transport in arid regions
730 or in clay soils, where liquid retention properties favor the development of high capillary
731 pressures.

732
733

734 **Acknowledgments**

735

736 We gratefully acknowledge the financial assistance received from the DGICYT of Spain,
737 under project FIS2005-07194 and from the Generalitat de Catalunya (2005SGR-00735). We
738 also acknowledge the support received from the DURSI and the European Social Fund.

739 **References**

740

- 741 [1] Abbasi F, Simunek J, Feyen J, van Genuchten MTh, Shouse PJ. Simultaneous inverse
742 estimation of soil hydraulic and solute transport parameters from transient field
743 experiments: homogeneous soil. *T ASAE* 2003;46(4):1085-95.
- 744 [2] Allred B, Brown GO. Boundary condition and soil attribute impacts on anionic
745 surfactant mobility in unsaturated soil. *Ground Water* 1996;34(6):964-71.
- 746 [3] Baggio P, Bonacina C, Schrefler BA. Some considerations on modeling heat and mass
747 transfer in porous media. *Transport Porous Med.* 1997;28:233-51.
- 748 [4] Bear J., Bachmat Y. Introduction to modeling of transport phenomena in porous media.
749 Dordrecht : Kluwer; 1991.
- 750 [5] Biggar JW, Nielsen DR. Spatial variability of the leaching characteristics of a field soil.
751 *Water Resour Res* 1976;1:78-84.
- 752 [6] Boufadel MC, Suidan MT, Venosa AD. Density-dependent flow in one-dimensional
753 variably-saturated media. *J Contam Hydrol* 1997;202:280-301.
- 754 [7] Boufadel MC, Suidan MT, Venosa AD. A numerical model for density-and-viscosity-
755 dependent flows in two-dimensional variably saturated porous media. *J Contam Hydrol*
756 1999;37:1-20.
- 757 [8] Brutsaert W. A theory for local evaporation (or heat transfer) from rough and smooth
758 surfaces at ground level. *Water Resour Res* 1975;11(4):543-50.
- 759 [9] Burdine NT. Relative permeability calculations from pore-size distribution data.
760 *Petroleum Trans* 1953;198:71-77.
- 761 [10] Chen D, Rolston DE, Yamaguchi T. Calculating partition coefficients of organic vapors
762 in unsaturated soil and clays. *Soil Science* 2000;165(3) 217-25.

- 763 [11] Chen D, Rolston DE, Moldrup P. Coupling diazinon volatilization and water evaporation
764 in unsaturated soils: I. Water transport. *Soil Science* 2000;165(9):681-89.
- 765 [12] Chen D, Rolston DE. Coupling diazinon volatilization and water evaporation in
766 unsaturated soils: II. Diazinon transport. *Soil Science* 2000;165(9):690-98.
- 767 [13] Friedel MJ. Documentation and verification of VST2D. A model for simulating transient,
768 variably saturated, coupled water-heat-solute transport in heterogeneous, anisotropic, 2-
769 dimensional, ground-water systems with variable fluid density. U.S. Geol. Surv. Water-
770 Resour. Invest.Rep. 00-4105, 2000.124 pp.
- 771 [14] Gammon BE, Marsh KN, Dewan AKR. Transport properties and related
772 thermodynamics data of binary mixtures. Part 1. New York: American Institute of
773 Chemical Engineers; 1993.
- 774 [15] Gawin D, Pesavento F, Schrefler BA. Modelling of hygro-thermal behaviour and damage
775 of concrete at temperature above the critical point of water. *Int J Numer Anal Meth*
776 *Geomech* 2002;26:537-62.
- 777 [16] Gmehling J, Onken U, Rarey-Nies JR., 1988. Vapor-liquid equilibrium data collection.
778 Aqueous systems. Vol. I, part 1b (Supplement 2). Frankfurt: DECHEMA; 1988.
- 779 [17] Grifoll J, Cohen Y. Contaminant migration in the unsaturated soil zone: the effect of
780 rainfall and evapotranspiration. *J Contam Hydrol* 1996;23:185-211.
- 781 [18] Grifoll J, Gastó JM, Cohen Y., Non-isothermal soil water transport and evaporation. *Adv*
782 *Water Resour* 2005;28(11):1254-66.
- 783 [19] Henry EJ, Smith JE, Warrick AW. Solubility effects on surfactant-induced unsaturated
784 flow through porous media. *J Hydrol* 1999;223:164-74.
- 785 [20] Henry EJ, Smith JE, Warrick AW. Surfactant effects on unsaturated flow in porous
786 media with hysteresis: horizontal column experiments and numerical modeling. *J Hydrol*
787 2001;245:73-88.

- 788 [21] Henry EJ, Smith, JE. The effect of surface-active solutes on water flow and contaminant
789 transport in variably saturated porous media with capillary fringe effects. *J Contam*
790 *Hydro* 2002;56:247-70.
- 791 [22] Henry EJ, Smith JE, Warrick AW. Two-dimensional modeling of flow and transport in
792 the vadose zone with surfactant-induced flow. *Water Resour Res* 2002;38(11):33-1 – 33-
793 16.
- 794 [23] Henry EJ, Smith JE. Surfactant-induced flow phenomena in the vadose zone: a review of
795 data and numerical modeling. *Vadose Zone J* 2003;2:154-67.
- 796 [24] Jaynes DB. Field study of bromacil transport under continuous-flood irrigation. *Soil Sci*
797 *Soc Am J* 1991;55:658-64.
- 798 [25] Jin Y, Jury A. Characterizing the dependence of gas diffusion coefficient on soil
799 properties. *Soil Sci Soc Am J* 1996;60:66-71.
- 800 [26] Kelley CT. Iterative methods for linear and nonlinear equations. Philadelphia: SIAM;
801 1995.
- 802 [27] Kyle BG. Chemical and process thermodynamics. New Jersey: Prentice Hall; 1999.
- 803 [28] Lenhard RJ, Oostrom M, Simmons CS, White MD. Investigation of density-dependent
804 gas advection of trichloroethylene: experiment and a model validation exercise. *J Contam*
805 *Hydro* 1995;19:47-67.
- 806 [29] Leverett MC, Capillary behavior in porous solids. *Trans AIME* 1941;142:152-69.
- 807 [30] Lide DR; Kehiaian HV. CRC Handbook of thermophysical and thermochemical data.
808 CRC Press; 1994.
- 809 [31] Morel-Seytoux HJ, Nimmo JR. Soil water retention and maximum capillary drive from
810 saturation to oven dryness. *Water Resour Res* 1999;35(7):2031-41.
- 811 [32] Nielsen DR, Biggar JW. Spatial variability of field-measured soil-water properties.
812 *Hilgardia* 1973;42(7):215-59.

- 813 [33] Ouyang Y, Zheng Ch. Density-driven transport of dissolved chemicals through
814 unsaturated soil. *Soil Science* 1999;164(6):376-90.
- 815 [34] Patankar SV. *Numerical heat transfer and fluid flow*. New York: McGraw-Hill; 1980.
- 816 [35] Press WH, Teukolsky SA, Vetterling WT, Flannery BP. *Numerical recipes in fortran 77:*
817 *the art of scientific computing*. New York: Cambridge University Press; 1986-1992.
- 818 [36] Rawls WJ, Brakensiek DL. Estimation of soil water retention and hydraulic properties.
819 *Unsaturated flow in hydrology modeling, theory and practice*. Kluwer Academic
820 Publishers; 1989.
- 821 [37] Reid RC, Prausnitz JM, Poling BE. *The properties of gases and liquids*. New York:
822 McGraw-Hill Inc.; 1987.
- 823 [38] Rossi C, Nimmo JR. Modeling of soil water retention from saturation to oven dryness.
824 *Water Resour Res* 1994;30(3):701-8.
- 825 [39] Rowlinson JS, Widom B. *Molecular theory of capillarity*. Oxford: Clarendon Press;
826 1984.
- 827 [40] Salvucci GD. Soil and moisture independent estimation of stage-two evaporation from
828 potential evaporation and albedo or surface temperature. *Water Resour Res*
829 1997;33(1):111-22.
- 830 [41] Schrefler BA. Multiphase flow in deforming porous material. *Int J Numer Anal Meth*
831 *Geomech* 2004;60:27-50.
- 832 [42] Shapiro AA, Stenby EH. Kelvin equation for non-ideal multicomponent mixture. *Fluid*
833 *Phase Equilibria* 1997;134:87-101.
- 834 [43] Smith JE, Gillham RW. The effect of concentration-dependent surface tension on the
835 flow of water and transport of dissolved organic compounds: a pressure head-based
836 formulation and numerical model. *Water Resour Res* 1994;30(2):343-54.

- 837 [44] Smith JE, Gillham RW. Effects of solute concentration-dependent surface tension on
838 unsaturated flow: laboratory sand column experiments. *Water Resour Res*
839 1999;35(4):973-82.
- 840 [45] Valsaraj KT. *Elements of environmental engineering. Thermodynamics and kinetics.*
841 Boca Raton: CRC Press Inc.; 1995.
- 842 [46] White MD, Oostrom M, Lenhard RJ. Modeling fluid flow and transport in variably
843 saturated porous media with the STOMP simulator. 1. Nonvolatile three-phase model
844 description. *Adv Water Resour* 1995;18(6):353-64.
- 845 [47] White MD, Oostrom M. *STOMP: Subsurface transport over multiple phases. Theory*
846 *guide.* PNNL-12030. Pac. Northw. Natl. Lab., Richland, WA; 2000.
- 847 [48] Zhang G, Zheng Z, Wan J. Modeling reactive geochemical transport of concentrated
848 aqueous solutions. *Water Resour Res* 2005;41(W02018):1-14.

849 **Table captions**

850

851 **Table 1.** Polynomial coefficients obtained by fit of experimental data at 20 °C to Eq. (19).

852

853 **Table 2.** Simulation conditions and hydraulic soil properties.

854

Table 1. Polynomial coefficients obtained by fit of experimental data[†] at 20 °C to Eq. (19)

Property	a_0	a_1	a_2	a_3	a_4	R^2
σ_i , (N m ⁻¹)	7.275×10^{-2}	-2.134×10^{-4}	5.352×10^{-7}	-6.831×10^{-10}	3.105×10^{-13}	0.996
ρ_i , (kg m ⁻³)	9.9701×10^2	-1.917×10^{-1}	1.665×10^{-4}	-3.340×10^{-7}	-	0.99994
μ_i , (kg m ⁻¹ s ⁻¹)	1.003×10^{-3}	3.134×10^{-6}	3.710×10^{-9}	-2.082×10^{-11}	1.298×10^{-14}	0.998
D_{ol}^m , (m ² s ⁻¹)	1.350×10^{-9}	-7.419×10^{-13}	-4.789×10^{-15}	8.486×10^{-18}	-	0.983

[†] Experimental data extracted from Gammon et al. [14].

Table 2. Simulation conditions and hydraulic soil properties

	Test case I	Test case II
	<u>Simulation conditions</u>	
Soil type	Sandy Clay Loam	Silty Clay
Soil depth (m)	0.5	0.5
Initial pressure head (m), P_{mi}	-100	-500
Infiltration rate (cm/h), q_{lo}	0.25	0.075
Total time of simulation (h)	72	168
Initial period of infiltration (h)	15	20
Dispersivity at saturation (cm), α_{Li}^o	0.2; 7.8	7.8
^a Atmosphere-side mass transfer coefficient for methanol (kg/m ² s), k_o^m	3.5×10^{-3}	3.5×10^{-3}
^a Atmosphere-side mass transfer coefficient for water (kg/m ² s), k_o^w	4.0×10^{-3}	4.0×10^{-3}
	<u>Hydraulic soil properties</u>	
^b Soil porosity, ε	0.33	0.423
^b Residual water content, θ_r	0.068	0.056
^b Brooks-Corey parameter, λ	0.25	0.127
^b Bubble pressure, P_{bw} (Pa)	2754	3352
^b Hydraulic saturated conductivity, K_s (cm/h)	0.43	0.09
^c Volumetric liquid content at junction, θ_j	0.1415	0.3079
^c Rossi-Nimmo parameter, α	0.0557	0.0756

^aCalculated according to Brutsaert [8] assuming a wind velocity of 2 m/s and a surface roughness length of 1 cm.

^bFrom Rawls and Brakensiek [36].

^cCalculated according to Morel-Seytoux and Nimmo [31].

Figure captions

Figure 1. Evolution in time of pressure head and liquid content at 38 cm depth for the infiltration in sand of a water-butanol solution at 7% w/w. Comparison of experimental and numerical simulation data of Smith and Gillham [44] with present numerical simulation.

Figure 2. Gas-liquid partition coefficients for methanol-water system.

Figure 3. Dependency of the concentration and liquid content at surface on (a) the grid spacing and (b) the maximum time step.

Figure 4. Infiltration and redistribution of methanol-water mixtures of different compositions into a Sandy Clay Loam soil. Simulation results after 48 hours and a dispersivity of 7.8 cm. (a) Volumetric liquid content. (b) Methanol concentration in the liquid-phase.

Figure 5. Evolution of normalized methanol volatilization and water evaporation fluxes for several infiltration methanol concentrations. (a) Volatilization of methanol. (b) Evaporation of water.

Figure 6. Liquid flux as function of methanol concentration decomposed into capillary and gravity components, after 48 hours of simulation. (a) Capillary liquid flux component. (b) Gravity liquid flux component.

Figure 7. Capillary liquid flux and its components after 48 hours of simulation, $C_{l,in} = 400 \text{ kg/m}^3$ and a dispersivity of 7.8 cm.

Figure 8. Normalized partial fluxes in a Sandy Clay Loam soil after 48 hours. (a) Diffusive partial flux of methanol in the gas-phase. (b) Dispersive partial flux of methanol in the liquid-phase. (c) Convective partial flux of methanol in the liquid-phase.

Figure 9. Infiltration and redistribution of methanol-water mixtures of different compositions into a Sandy Clay Loam soil. Simulation results after 48 hours and a dispersivity of 0.2 cm. (a) Volumetric liquid content. (b) Methanol concentration in the liquid-phase.

Figure 10. Capillary liquid flux and its components after 48 hours of simulation, $C_{l,in} = 400 \text{ kg/m}^3$ and a dispersivity of 0.2 cm.

Figure 11. Profiles after infiltration, redistribution and volatilization of a methanol-water mixture into a Silty Clay soil (dotted line for results ignoring Kelvin effect within the soil). (a) Volumetric liquid content. (b) Methanol concentration in the liquid-phase.

Figure 12. Kelvin effect on normalized partial fluxes in a Silty Clay soil after 168 hours and $C_{l,in} = 400 \text{ kg/m}^3$ (dotted line for results ignoring Kelvin effect within the soil). (a) Diffusive partial flux of methanol in the gas-phase. (b) Diffusive partial flux of water in the gas-phase.

Figure 13. Kelvin effect on methanol volatilization and water evaporation from a Silty Clay soil (dotted line for results ignoring Kelvin effect within the soil). (a) Volatilization of methanol. (b) Evaporation of water.

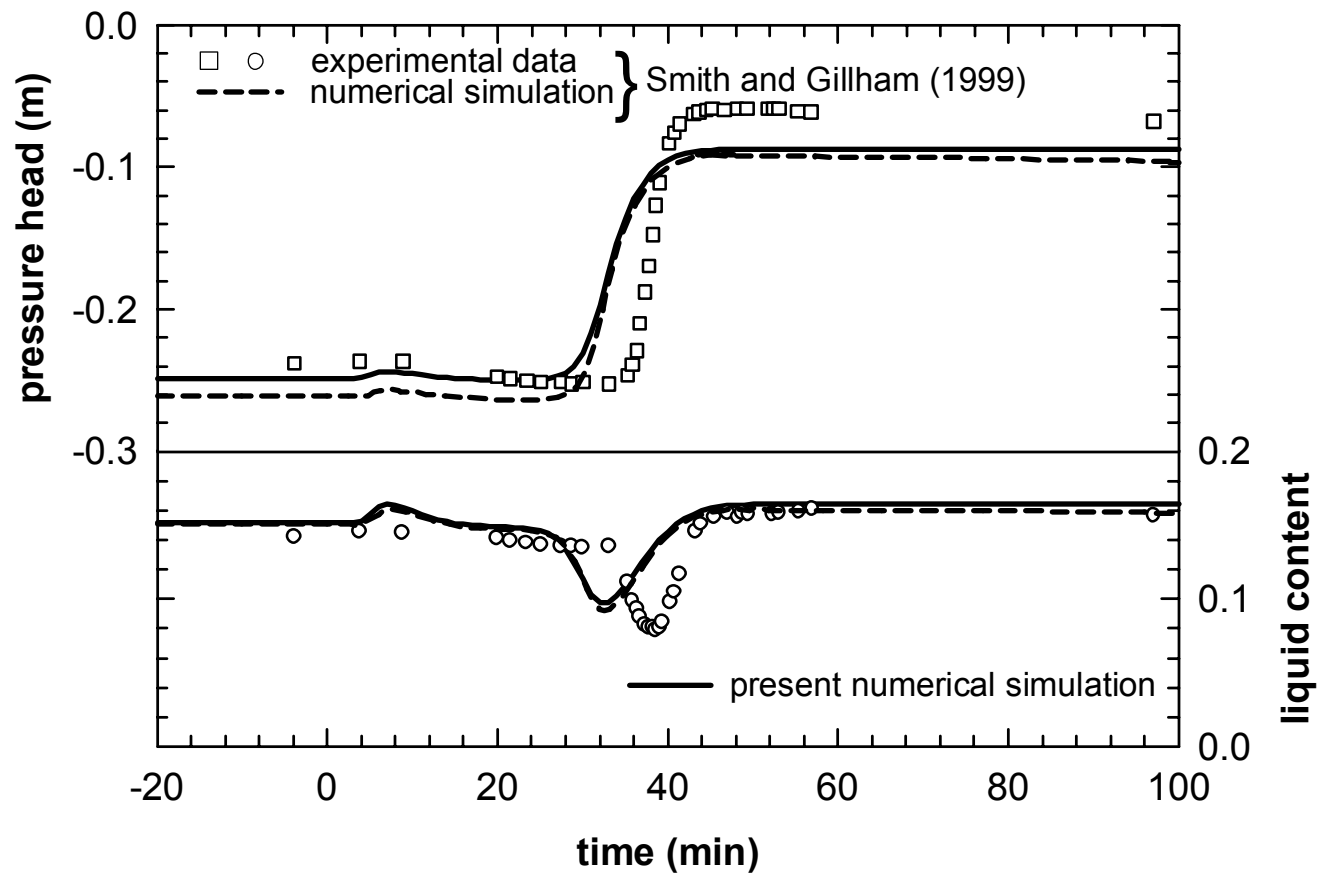


Figure 1

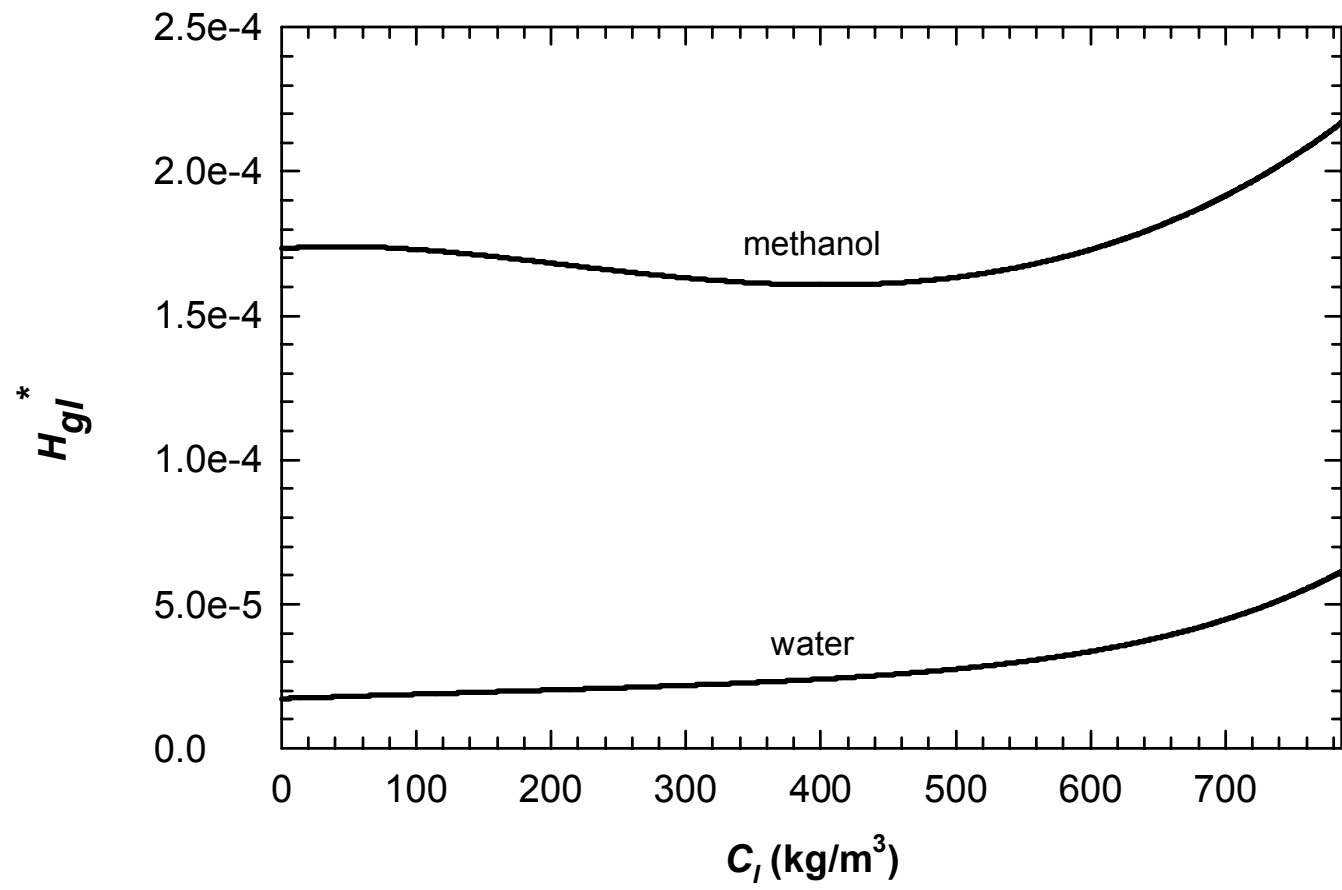


Figure 2

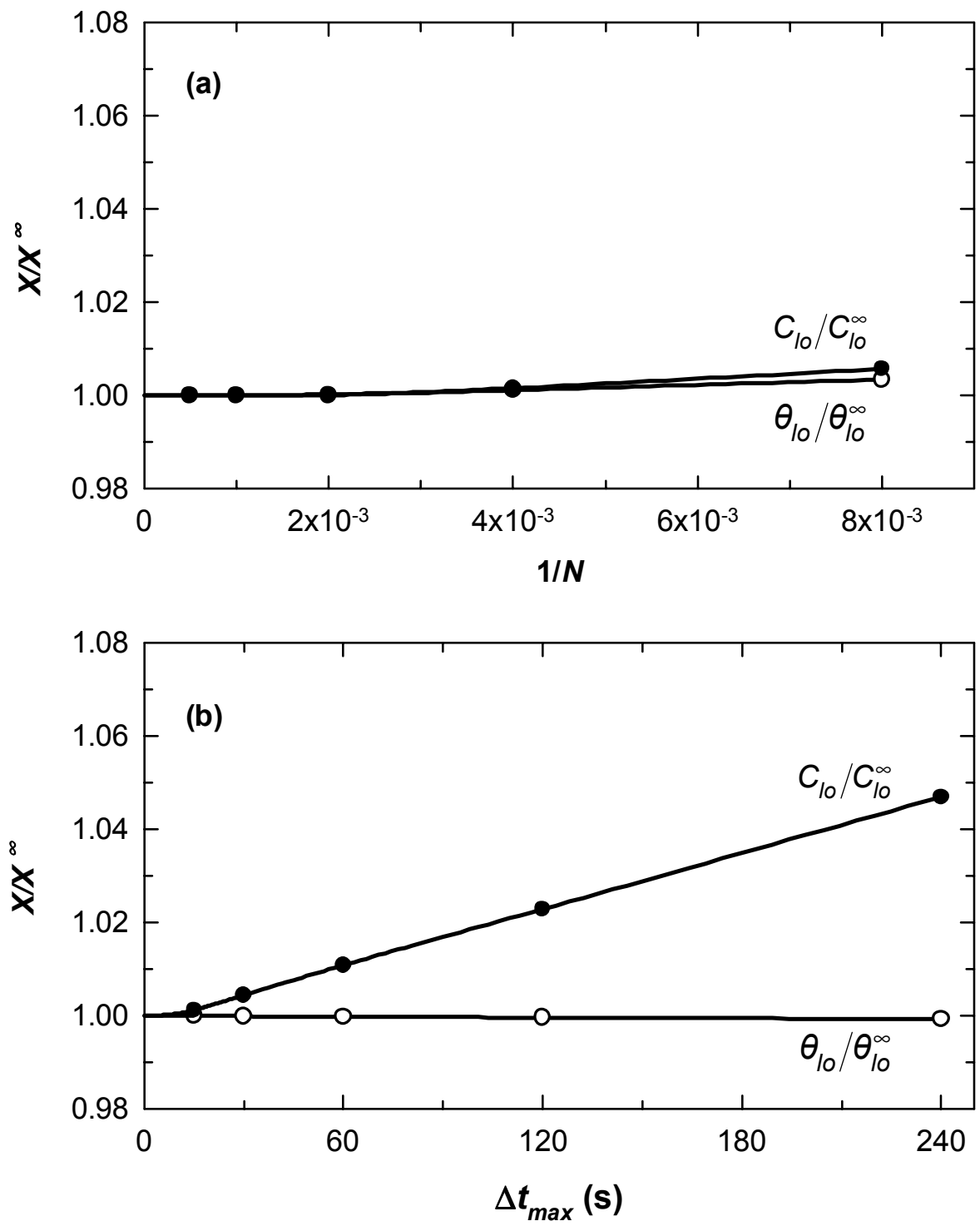


Figure 3

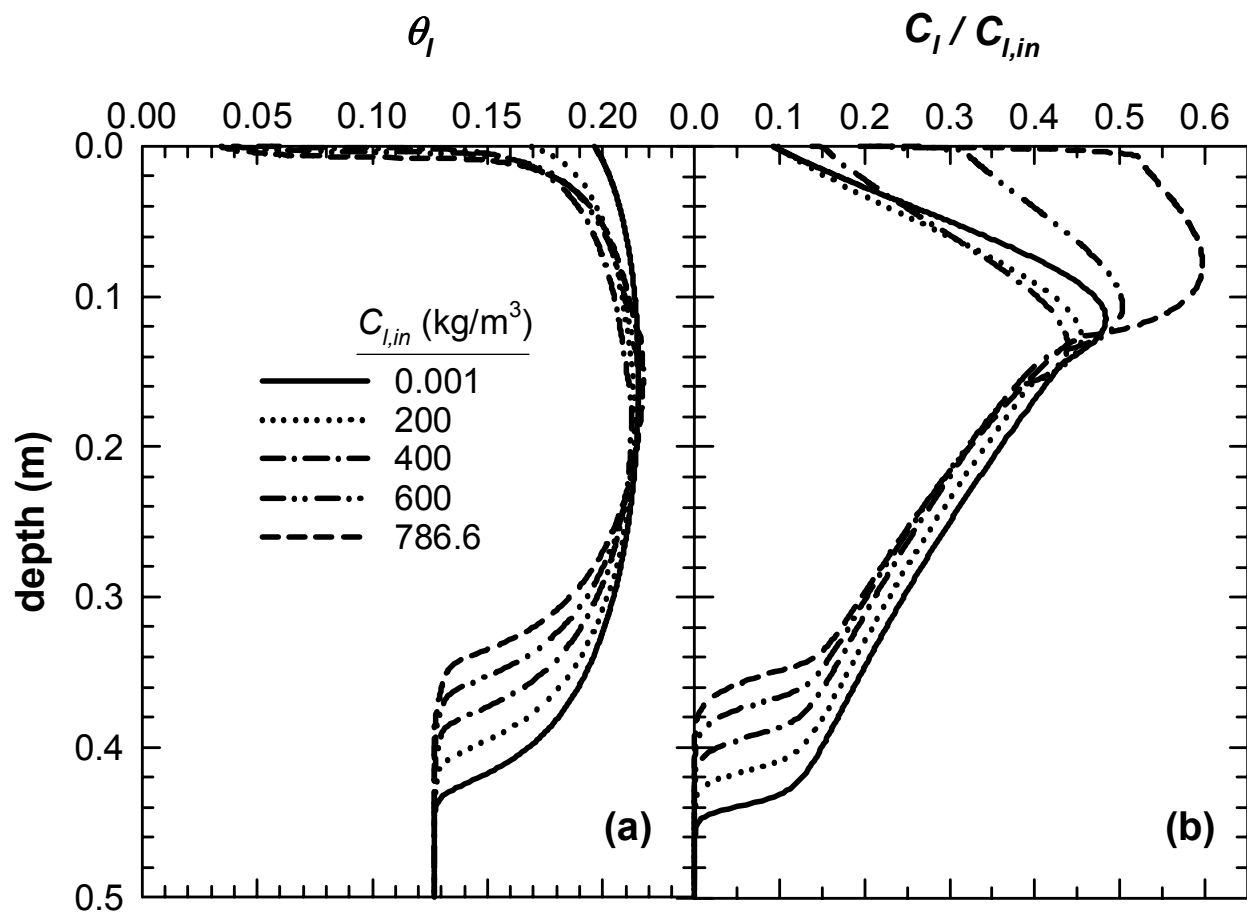


Figure 4

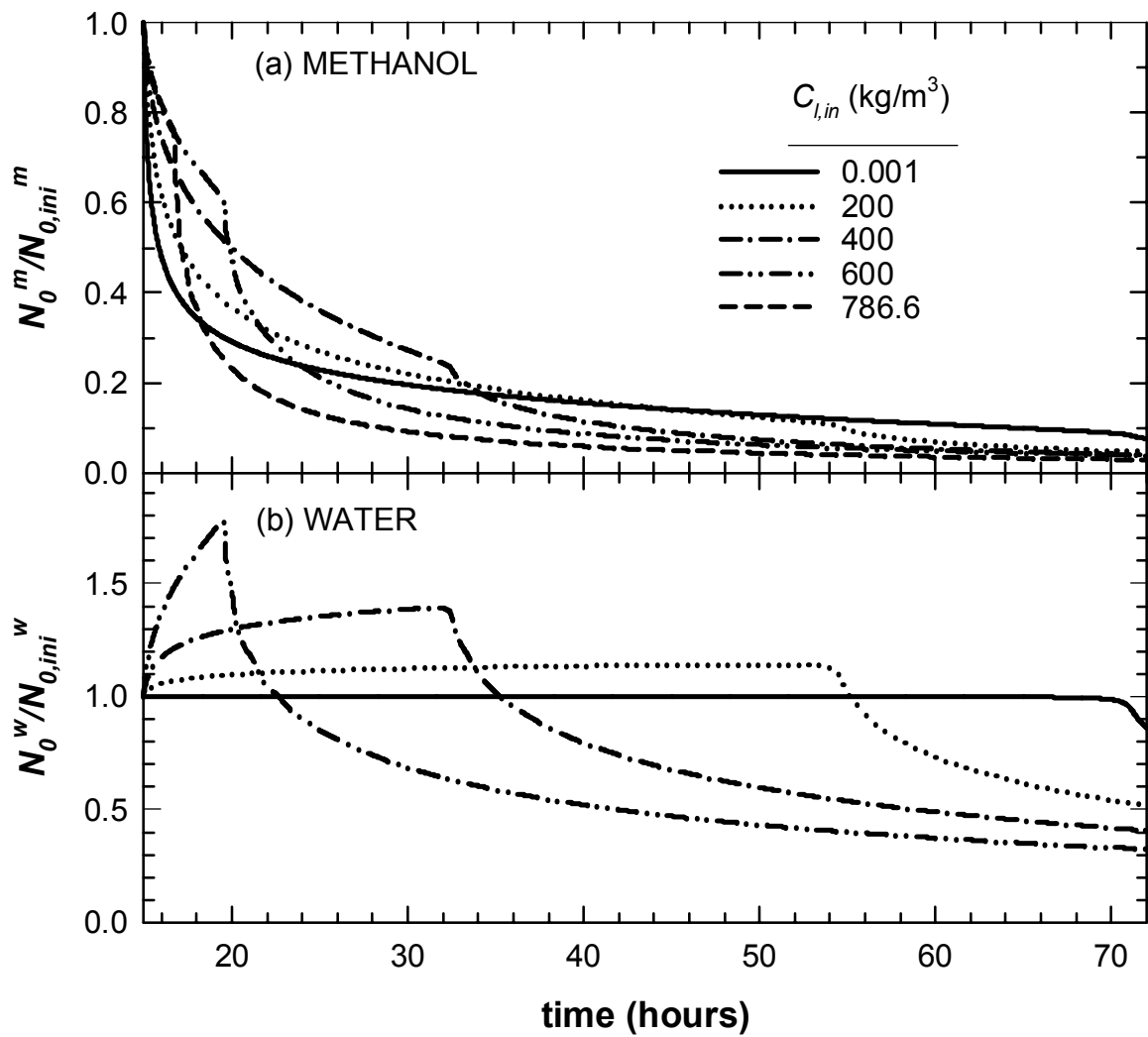


Figure 5

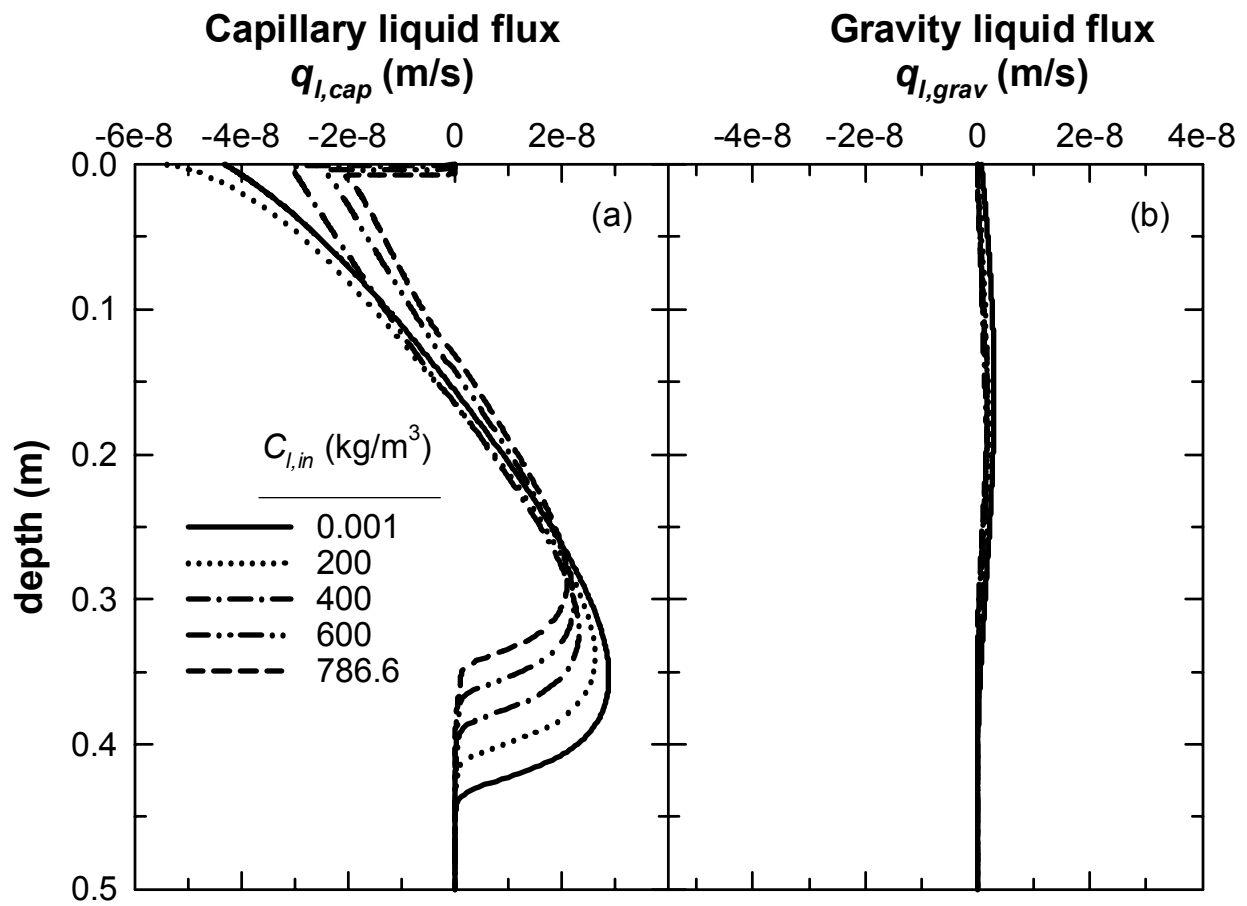


Figure 6

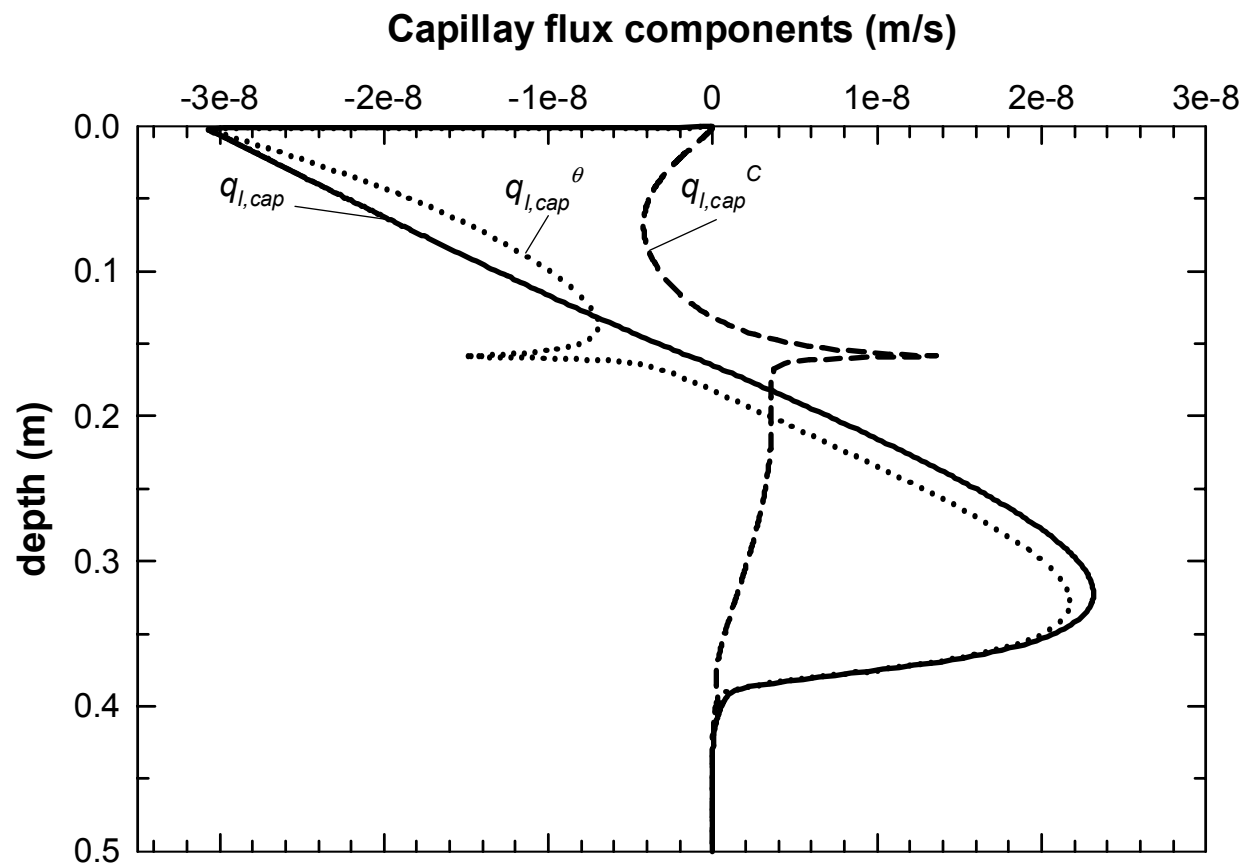


Figure 7

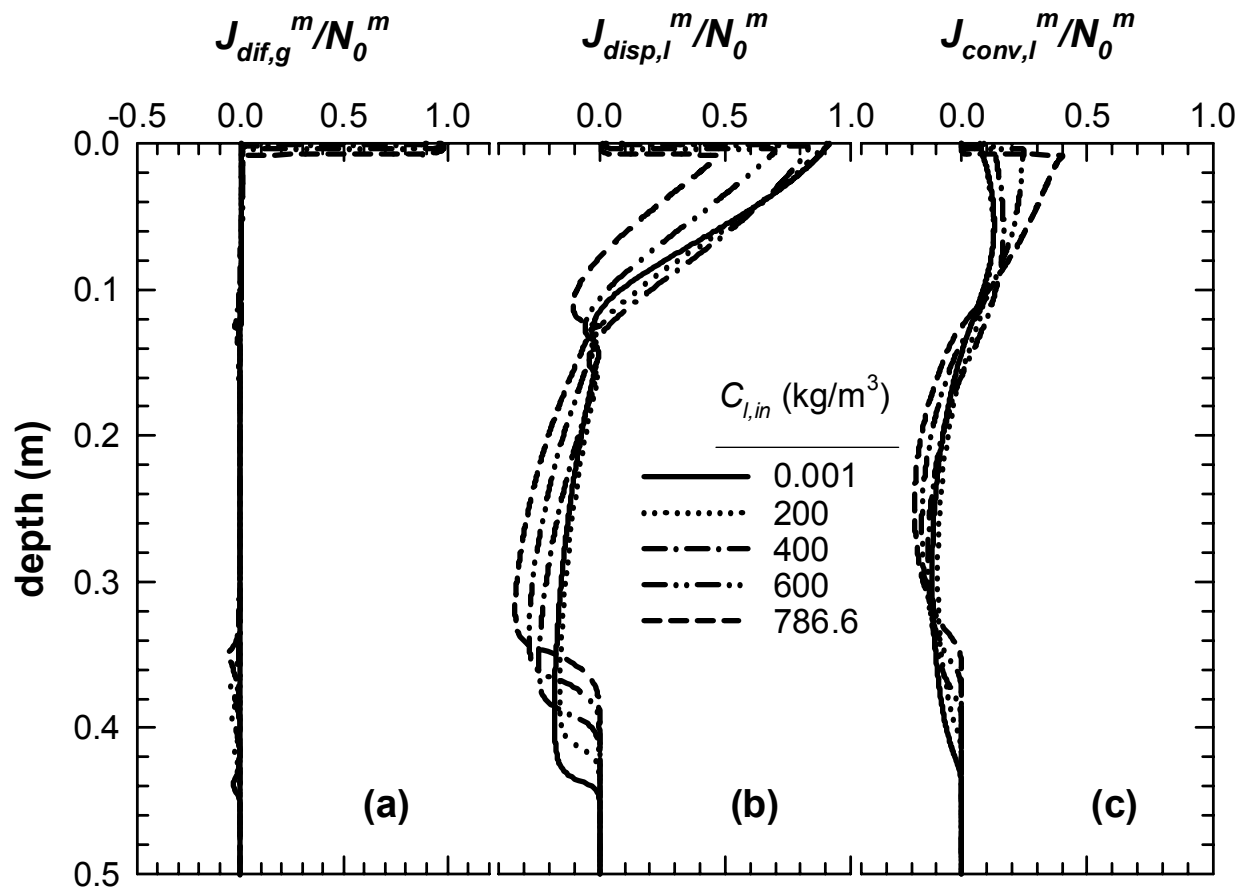


Figure 8

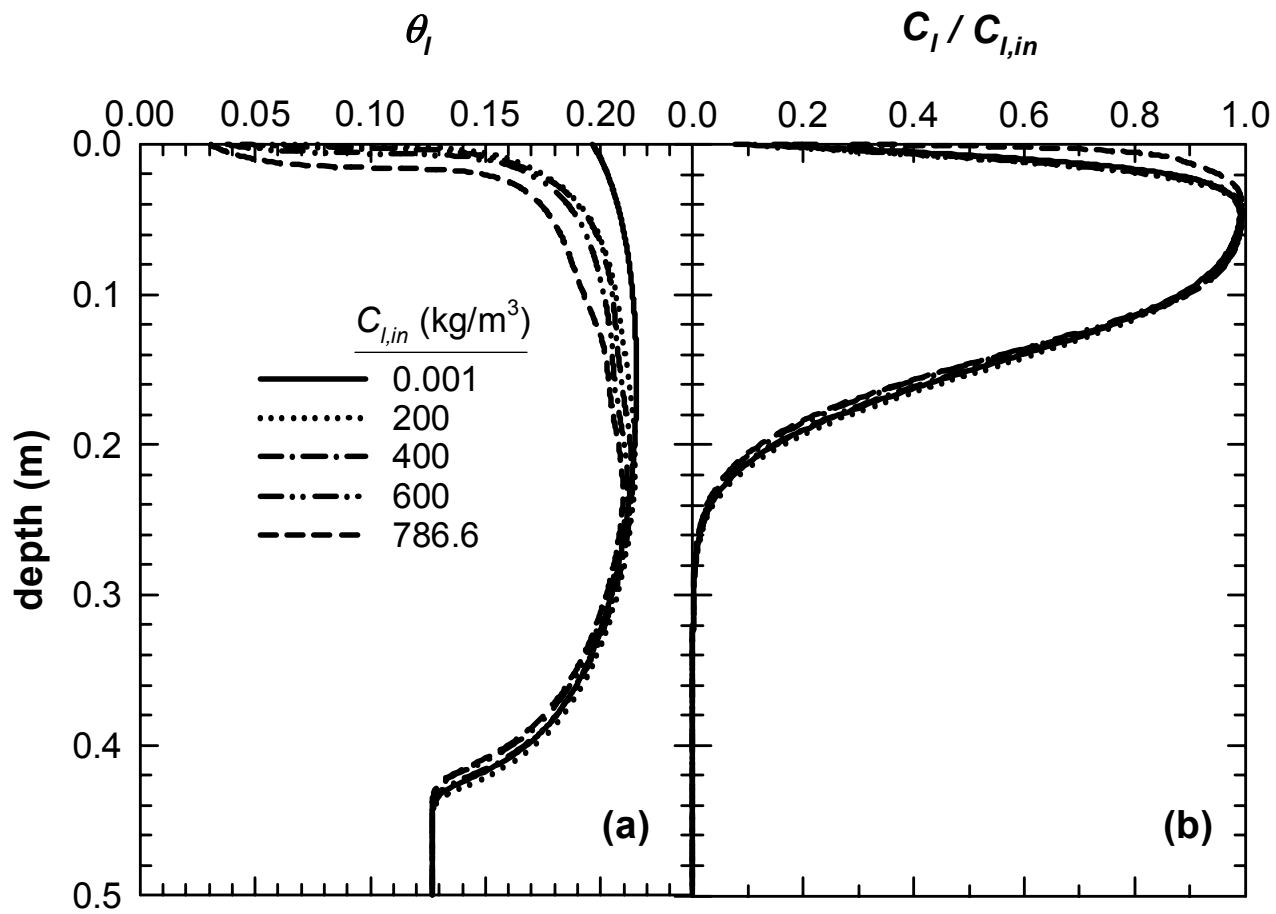


Figure 9

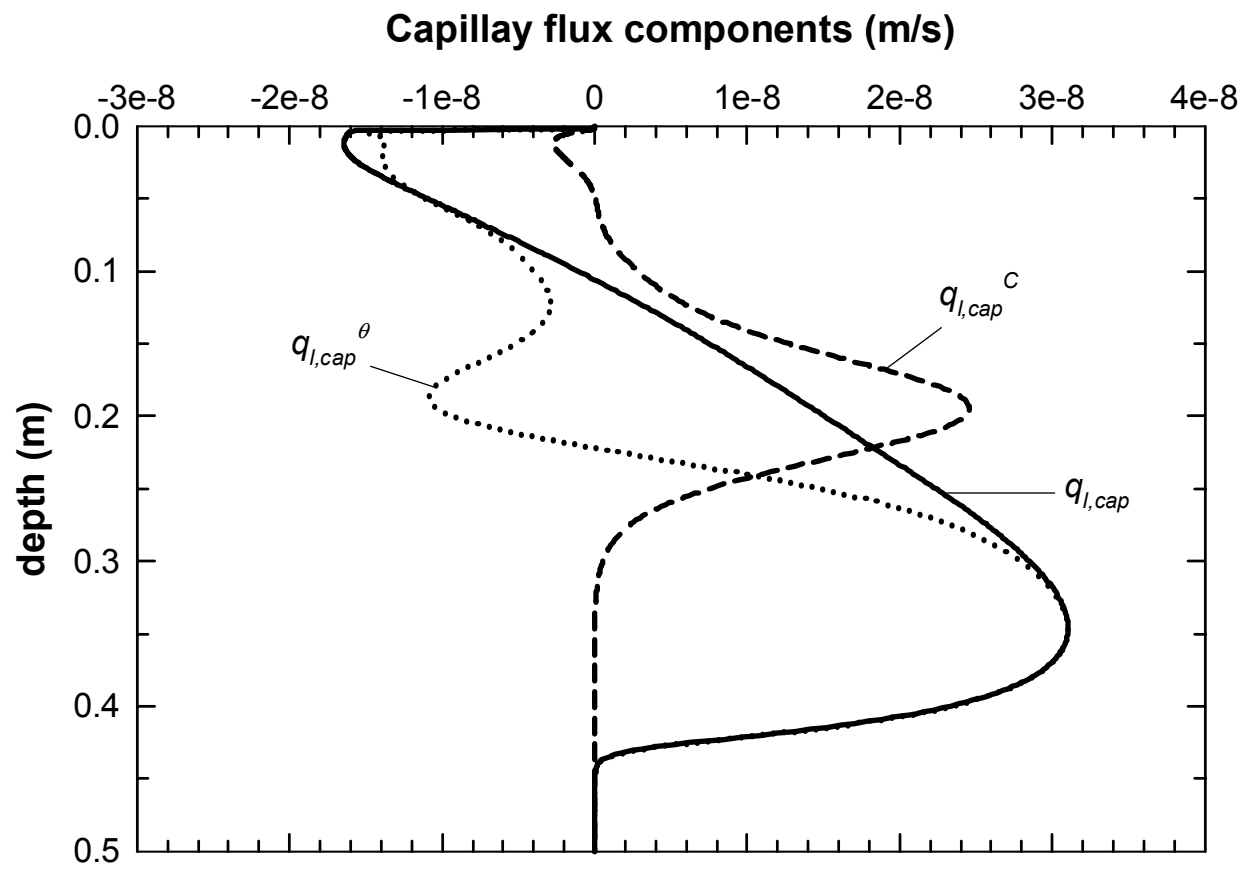


Figure 10

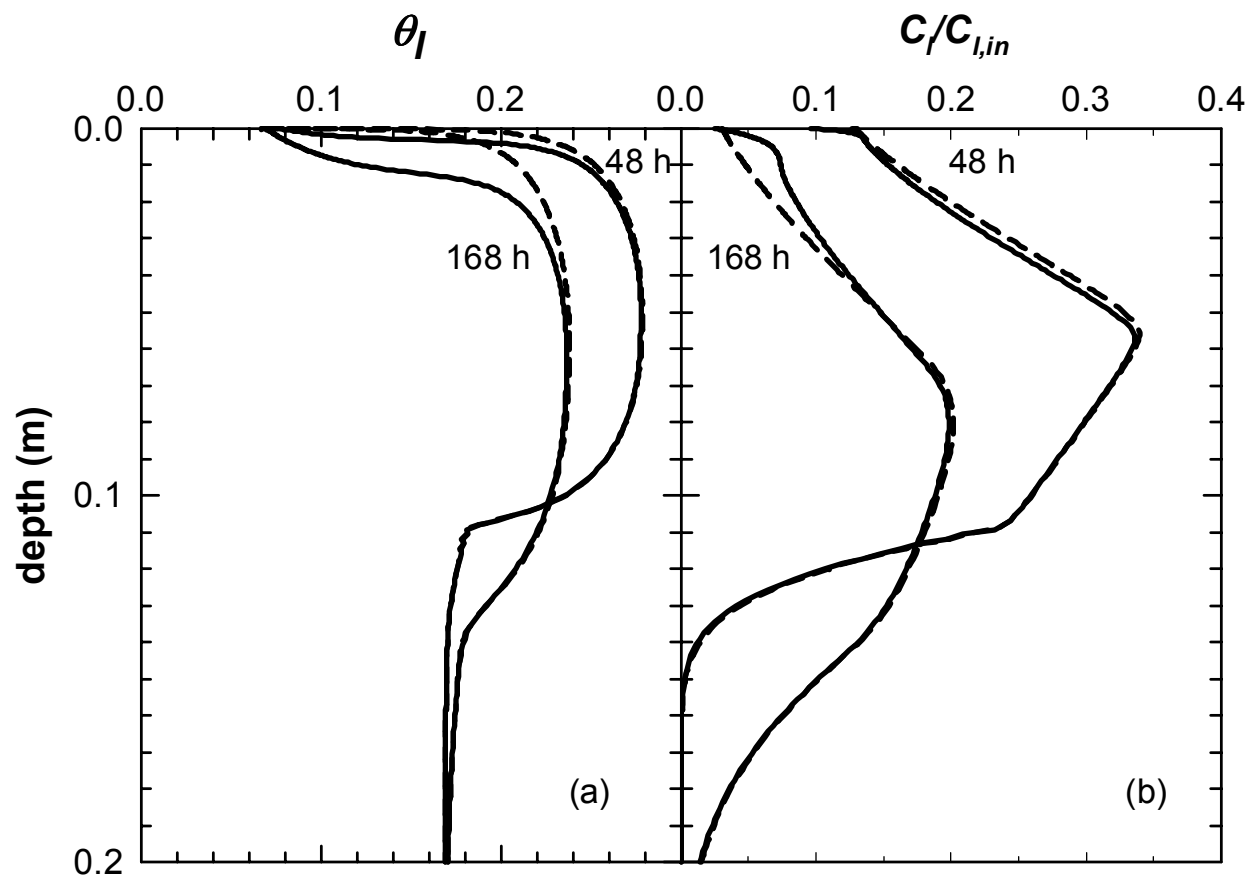


Figure 11

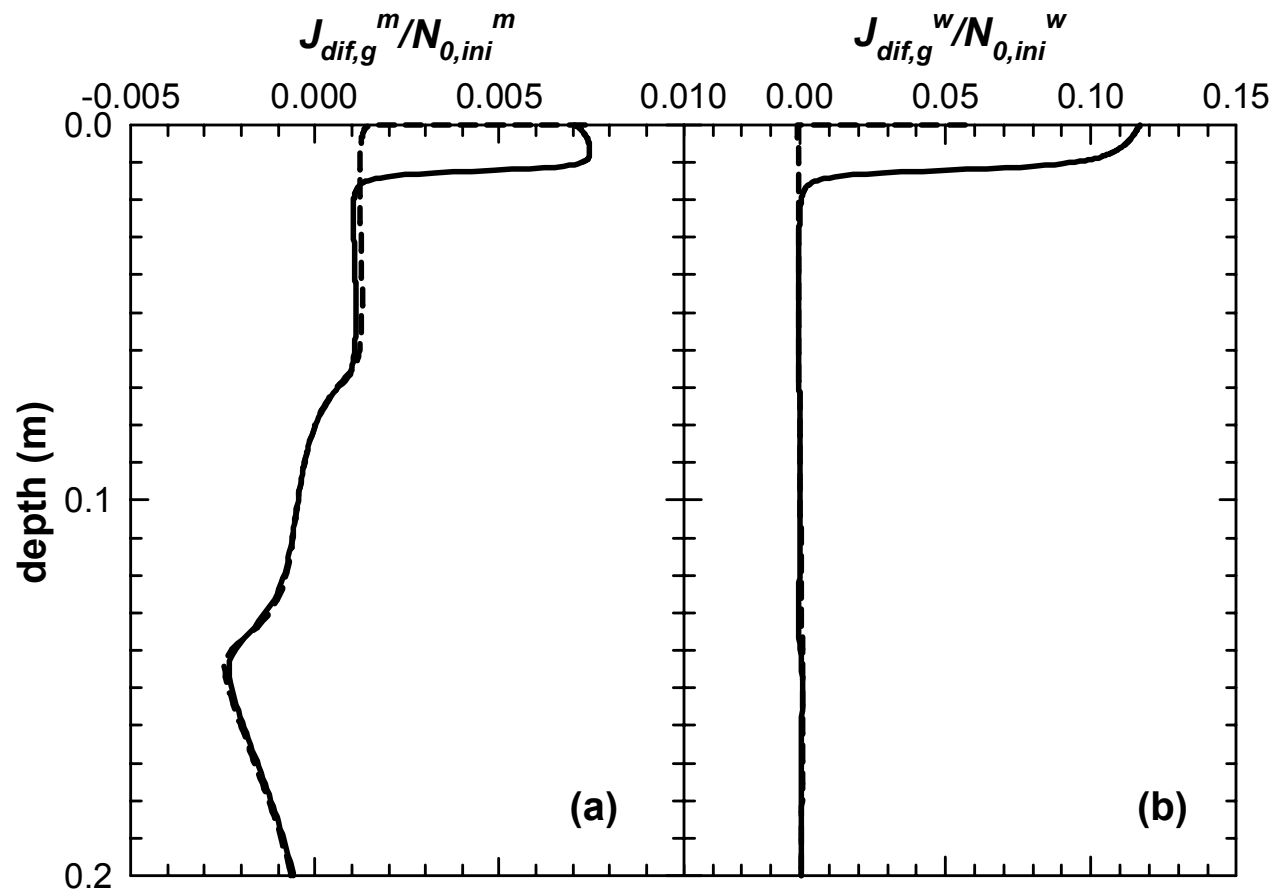


Figure 12

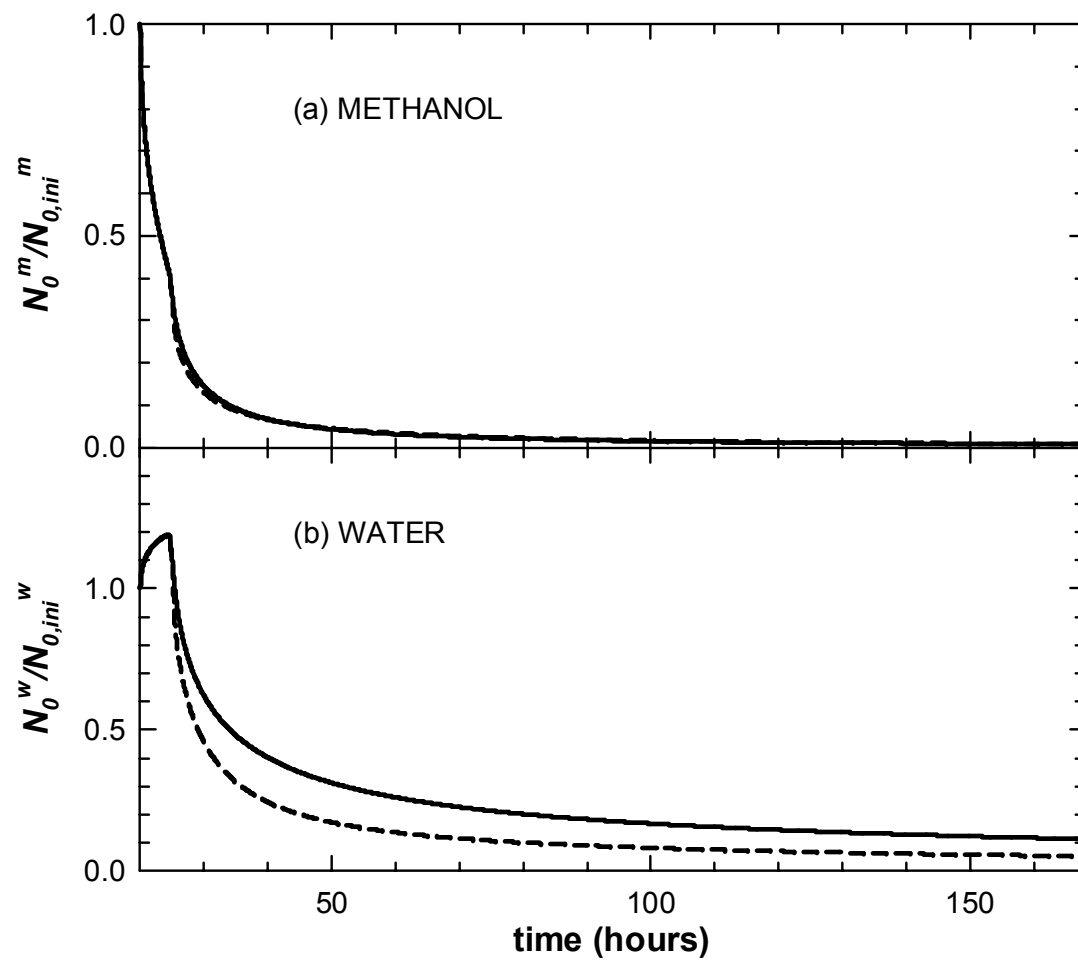


Figure 13